

## Kinematic history of the Laramide orogeny in latitudes 35°-49°N, western United States

Peter Bird

Department of Earth and Space Sciences, University of California, Los Angeles

**Abstract.** The kinematic history of the Rocky Mountain foreland and adjacent areas is computed back to 85 Ma, using virtually all the structural, paleomagnetic, and stress data in the literature. A continuous velocity field is fit to the data in each time step by weighted least squares, and this velocity is integrated back through time. As proposed by *Hamilton* [1981], the net movement of the Colorado Plateau was a clockwise rotation about a pole in northern Texas; but the rotation was less (3°) than some have inferred from paleomagnetism. The Laramide orogeny occurred during 75-35 Ma, with peak Colorado Plateau velocities of 1.5 mm yr<sup>-1</sup> during 60-55 Ma. The mean azimuth of foreland velocity and mean direction of foreland shortening was stable at 40° for most of the orogeny, increasing to 55° in 50-40 Ma; the counter-clockwise rotation of shortening directions proposed by some previous authors is incorrect. Comparing the computed histories of foreland flow speed and direction with the known motions of the Kula and Farallon plates confirms that the Laramide orogeny had a different mechanism from the early Sevier orogeny: it was driven by basal traction during an interval of horizontal subduction, not by edge forces due to coastal subduction or the spreading of the western cordillera or by accretion of terranes to the coast. Tentatively, a minor clockwise rotation of shortening directions at 50 Ma may record the passage of an active Kula-Farallon transform within the subducted slab.

### 1. Introduction

The west central part of the United States (Figure 1) has been deformed by three overlapping events since Cretaceous time. The Sevier orogeny lasted from about 119 Ma [*Heller and Paola*, 1989] to 50 Ma [*DeCelles and Mitra*, 1995] and resulted in displacement of thick plates of sedimentary rock eastward for tens of kilometers on bedding-plane thrusts with west dipping ramps. The Laramide orogeny lasted from about 75 to 35 Ma [*Dickinson et al.*, 1988] and involved thrusting of the Precambrian metamorphic basement in a variety of directions on faults of 25°-30° dip with throws up to 13 km. Extension began about 49 Ma [*Constenius*, 1996] in the former Sevier orogenic belt, and after 29 Ma it also affected the Rocky Mountain foreland in New Mexico and Colorado where the Rio Grande rift was formed.

The Laramide orogeny did not involve large strains or displacements, but it is of particular interest for several reasons.

First, it occurred in a plate interior, so it has no simple explanation in terms of plate tectonics. Second, it occurred in a region with a continuous cover of Phanerozoic section whose surface was initially near sea level, so that all strains and uplifts are especially well recorded. Third, the literature on this subject is mature, and the chance for future discoveries of first-order structures seems small. The Laramide orogeny is the primary focus of this paper, although the calculation necessarily includes those parts of the Sevier orogeny and the Tertiary extension that overlapped it.

During this time, eastern North America was stable. Oceanic lithosphere was subducting at the western margin of North America, as it had been since the Jurassic. The Kula plate was subducting along the north part of the margin, and the Farallon plate was subducting along the south part; the past history of the triple junction between them is controversial [*Engebretson et al.*, 1985]. This subduction may have influenced the Rocky Mountain foreland by generating horizontal stresses in the lithosphere at the margin. Alternatively, there may have been an episode of horizontal subduction of one or both oceanic plates, allowing direct stress transfer to the base of the lithosphere in the foreland [*Dickinson and Snyder*, 1978]. A major goal of this paper is to refine the kinematics so as to permit testing of these hypotheses.

In this paper, I apply a new algorithm to compute the kinematics of the orogeny in time steps of 5 m.y. back to 85 Ma. The details of the method are described in Appendix A. Broadly, however, the algorithm has the five following steps: (1) Geologic and paleomagnetic data concerning finite displacements, rotations, or strains over long time periods are converted to rate estimates. An uncertainty is assigned to each rate estimate. (2) The velocities of all the nodes in a finite element grid are determined by solving a linear system, which is based on weighted least squares fitting of the velocity model to the tentative rates. (3) These velocities are integrated backward over time, using 5 m.y. steps. The program moves the nodes of the finite element grid, the present state lines, or other fiducial markers and the positions of all data concerning earlier times. In particular, paleostress indicators are restored to their original azimuths. (4) When the history is complete, each geologic and paleomagnetic datum on finite strain, displacement, or rotation is compared to the history predicted by the model. In general, the model rate of strain, displacement, or rotation will not be uniform over the time window of the datum, as initially assumed. New target rates are now assigned, based on the time-history from the previous model but adjusted by a factor to achieve the correct total strain, displacement, or rotation. (5) The entire computation is now repeated, beginning with step 2. In all, 50 iterations of the history were performed.

Copyright 1998 by the American Geophysical Union.

Paper number 98TC02698.  
0278-7407/98/98TC-02698\$12.00

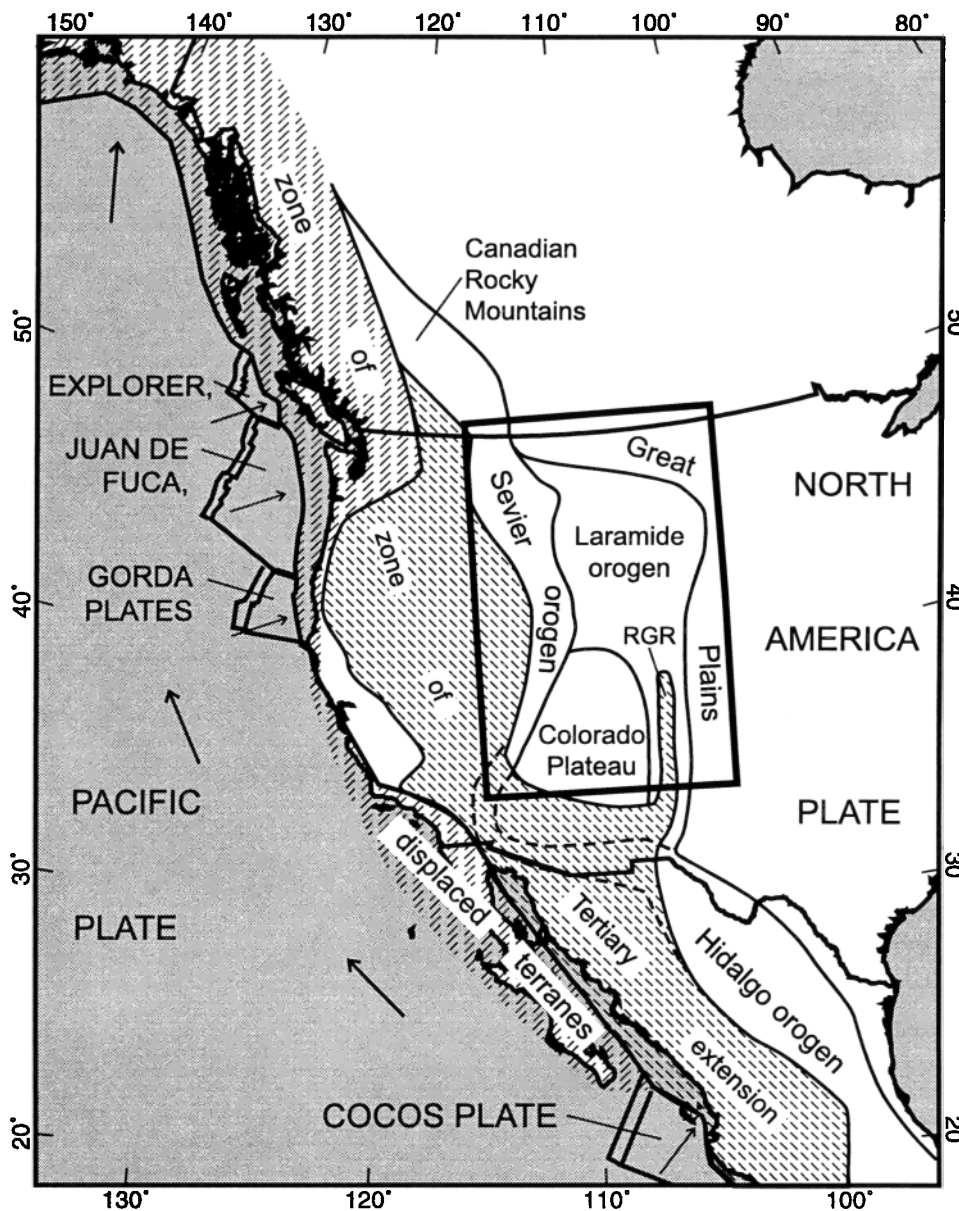


**Figure 1.** Location of the Laramide orogen in relation to other Cretaceous-Tertiary tectonic provinces in present coordinates. The Great Plains is the upwarped margin of the stable part of the North America plate. The Laramide orogen (or Rocky Mountain foreland) is a region of basement thrusts overlain by forced folds. The Colorado Plateau has similar structure but underwent less strain. The Sevier orogen (or Sevier belt or Overthrust belt) contains east vergent ramp/flat thrusts in thick sedimentary sequences. The Canadian Rocky Mountains are similar in structure to the Sevier orogen. The Hidalgo orogen is intermediate in character between the Laramide and the Sevier and may be structurally connected to both (dashed lines). The zone of Tertiary extension includes the Basin and Range province and the Rio Grande rift (RGR). The zone of displaced terranes includes Baja California and allocthanous terranes in British Columbia and Washington. The Explorer, Juan de Fuca, Gorda, and Cocos plates are remnants of the large Farallon plate. Bold rectangle shows the study area and location of Figures 2-6.

At the end of the computation, we have estimated histories of the slip on each fault and the drift and rotation of each paleomagnetic site. More important, we have an estimated velocity field through time for the whole region, which can be examined for insights into the ultimate causes of the orogeny and its relation to nearby events in North America and/or the Pacific basin.

This method is a type of "inverse" tectonic modeling, which computes velocities from geologic data. It is conceptually and procedurally distinct from previous efforts to model the Laramide orogeny [Bird, 1988, 1989, 1992], which were "forward" or "dynamic" models based on physics and assumed rheologies. Inverse tectonic modeling is relatively new. Saucier and Humphreys [1993] modeled velocities in

California from fault slip rates and geodesy. *Holt and Haines* [1993] used seismicity to solve for a continuous velocity field in Asia, while *Avouac and Tapponnier* [1993] divided Asia into four rigid blocks, and *Peltzer and Saucier* [1996] modeled its fault network in more detail. In comparison, this method is unique in its ability to handle long histories, finite strain, many faults, paleomagnetic data, and stress-direction data.

## 2. Data and Computation

The first application of this method is a solution for the Rocky Mountain foreland province of the western United States (latitudes 35°-49°N, longitudes 103°-113°W) since 85 Ma (Santonian). I chose this region for an initial trial because the tectonics are relatively simple and noncontroversial and because they are described in a mature literature of manageable size.

I attempted to collect all the significant information from the geologic literature through the end of 1997. While reading, I excluded estimates of age or strain that were based on regional consistency arguments, so that the requirement of independent errors for each datum might be fulfilled. Useful data were found in 262 papers; their bibliographic citations are listed in one of the files described in Appendix B. This data set is rich in fault offsets (307 faults) and has a good number of paleomagnetic sites (220), but has fewer stress indicators (71 sites) and only a few balanced cross sections (11). Most of the fault offsets (Figure 2) are dip-slip; although I include all the dextral strike-slip faults proposed by *Chapin and Cather* [1981] or by *Chapin* [1983], their joint offset is limited to about 20 km by the stratigraphic constraints of *Woodward et al.* [1997]. Where the literature specifies amounts of crustal shortening or extension across dip-slip faults, these figures are used directly. When only the stratigraphic throw was available, it is converted to horizontal motion by assuming fault dips of 25° for thrusts and 65° for normal faults.

Paleomagnetic paleolatitude anomalies and vertical-axis rotations are derived from the database of *McElhinny and Lock* [1995], using only rocks magnetized since 85 Ma. I exclude samples with secondary magnetizations, those with unknown structural corrections, and all sedimentary rocks (because of the possibility of compaction-induced inclination anomalies). The North America polar wander path used to compute anomalies is from *Van Alstine and de Boer* [1978]. None of the paleolatitude anomalies exceeds twice the size of its standard deviation, and probably none of them is significant. Most of the computed vertical-axis rotations are less than 34° (except in some thrust plates of the Sevier belt). Therefore it is not surprising that there are few features of the solution driven entirely by paleomagnetic results.

Because of the shortage of conventional stress indicators for some of the time steps in this application, I treat faults as additional stress indicators (in their first phase of movement), with the greatest horizontal principal compression normal to thrusts and parallel to normal faults. Each of these rather unreliable stress indicators is assigned a 90% confidence range of  $\pm 45^\circ$ .

The finite element grid has 787 elements of mean area  $1.6 \times 10^9 \text{ m}^2$ . It is fixed to the velocity reference frame of

eastern North America on the eastern side and on the eastern part of the northern side. The history back to 85 Ma was computed using 5 m.y. time steps. This history was iterated 50 times, using initial rate uncertainties ( $\sigma^*$ ) of  $4 \times 10^{-12} \text{ m s}^{-1}$  ( $0.12 \text{ mm yr}^{-1}$ ) for fault offsets and balanced cross-section extensions,  $2 \times 10^{-10} \text{ m s}^{-1}$  ( $0.06^\circ \text{ m.y.}^{-1}$ ) for paleolatitude shifts, and  $1.4 \times 10^{-16} \text{ radians/s}$  ( $0.25^\circ \text{ m.y.}^{-1}$ ) for vertical-axis rotations. In a typical iteration, about 30% of the rate histories were automatically adjusted; cumulatively, 64% were adjusted. (As discussed in Appendix A, some rate histories cannot be adjusted because of the danger of numerical instability.) The rate uncertainties in the final iterations were based only on the individual uncertainties in displacement or rotation tabulated in the files named in Appendix B. The uncertainty in the nominally zero strain rate of regions without active faults was  $5 \times 10^{-17} \text{ s}^{-1}$  ( $0.16\% \text{ m.y.}^{-1}$ ) in the Rocky Mountain foreland and Great Plains but slightly larger ( $1 \times 10^{-16} \text{ s}^{-1}$ ) in the Sevier belt, and was largest ( $2 \times 10^{-16} \text{ s}^{-1}$ ) in areas now obscured by volcanic cover of the Yellowstone-Snake River Plain hotspot (blank area in Figure 2).

At the conclusion of the 50 iterations, all model predictions were compared to corresponding offset, strain, or rotation data to check the size of residuals. These were generally of acceptable size, measured in terms of the assigned uncertainties of the data. Fault offset data were fit with an RMS residual of 0.91 standard deviation and an average residual of 0.39 standard deviation; 5% of residuals exceeded two standard deviations. Paleolatitude anomalies were fit with an RMS residual of 0.81 standard deviation and an average residual of 0.67 standard deviation; none exceeded two standard deviations. Vertical-axis rotations were not fit quite as well, with an RMS residual of 1.34 standard deviations and an average residual of 1.05 standard deviations; 12% of residuals exceeded two standard deviations. Overall, the built-in "reasonableness" constraints of consistent stress direction and minimum deformation in unfaulted areas did not prevent the model from fitting the data within its assigned uncertainties.

## 3. Results

Velocities and fault slip rates from selected times in the solution are shown in Figures 3 through 6. As expected, the continuing Sevier orogeny in the Overthrust Belt of Montana-Idaho-Wyoming-Utah is the only activity during the 85-75 Ma time steps. The Laramide orogeny began during 75-70 Ma with thrusting concentrated in western Wyoming. It expanded eastward to the Black Hills of South Dakota-Wyoming by 55 Ma. Rates of thrusting in the foreland peaked during 60-55 Ma and then declined smoothly to an end during 40-35 Ma. These general patterns are well known and can be inferred without modeling; therefore the rest of this discussion will focus on details of the velocity field, which is the most novel result.

One of the most notable features is a clockwise rotation of the Colorado Plateau region during 75-50 Ma, the time of the highest velocity magnitudes. Since the Plateau simultaneously moved NE, its net motion with respect to stable North America since 85 Ma can be described as a clockwise rotation of  $2.6^\circ$ - $3.1^\circ$  about an Euler pole near ( $34^\circ\text{N}$ ,  $103^\circ\text{W}$ ) in the northern part of Texas. This is almost exactly the result of

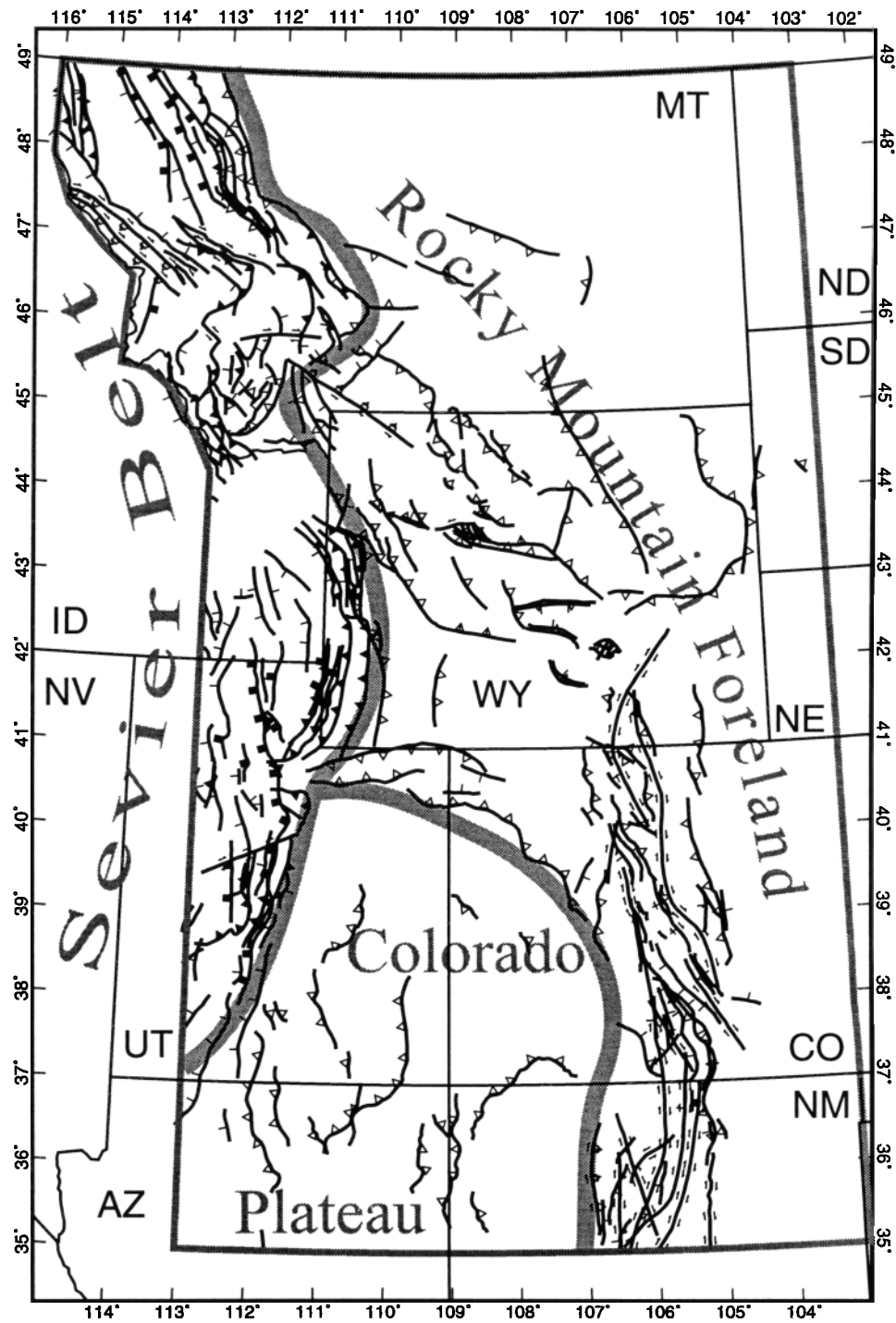


**Figure 2.** Location map with traces of 307 Late Cretaceous-Tertiary faults used in this computation. Medium shaded line is the outer boundary of the finite element grid and model region. Wide shaded lines approximately separate the Sevier belt, Colorado Plateau, and Rocky Mountain foreland regions for purposes of discussion. The area with no faults around (44°N, 112°W) is obscured by volcanic cover of the Snake River Plain-Yellowstone hotspot track. Abbreviations for states are as follows: AZ, Arizona; CO, Colorado; ID, Idaho; MT, Montana; ND, North Dakota; NE, Nebraska; NM, New Mexico; NV, Nevada; SD, South Dakota; UT, Utah; WY, Wyoming. This is a transverse Mercator projection with prime meridian 109°W.

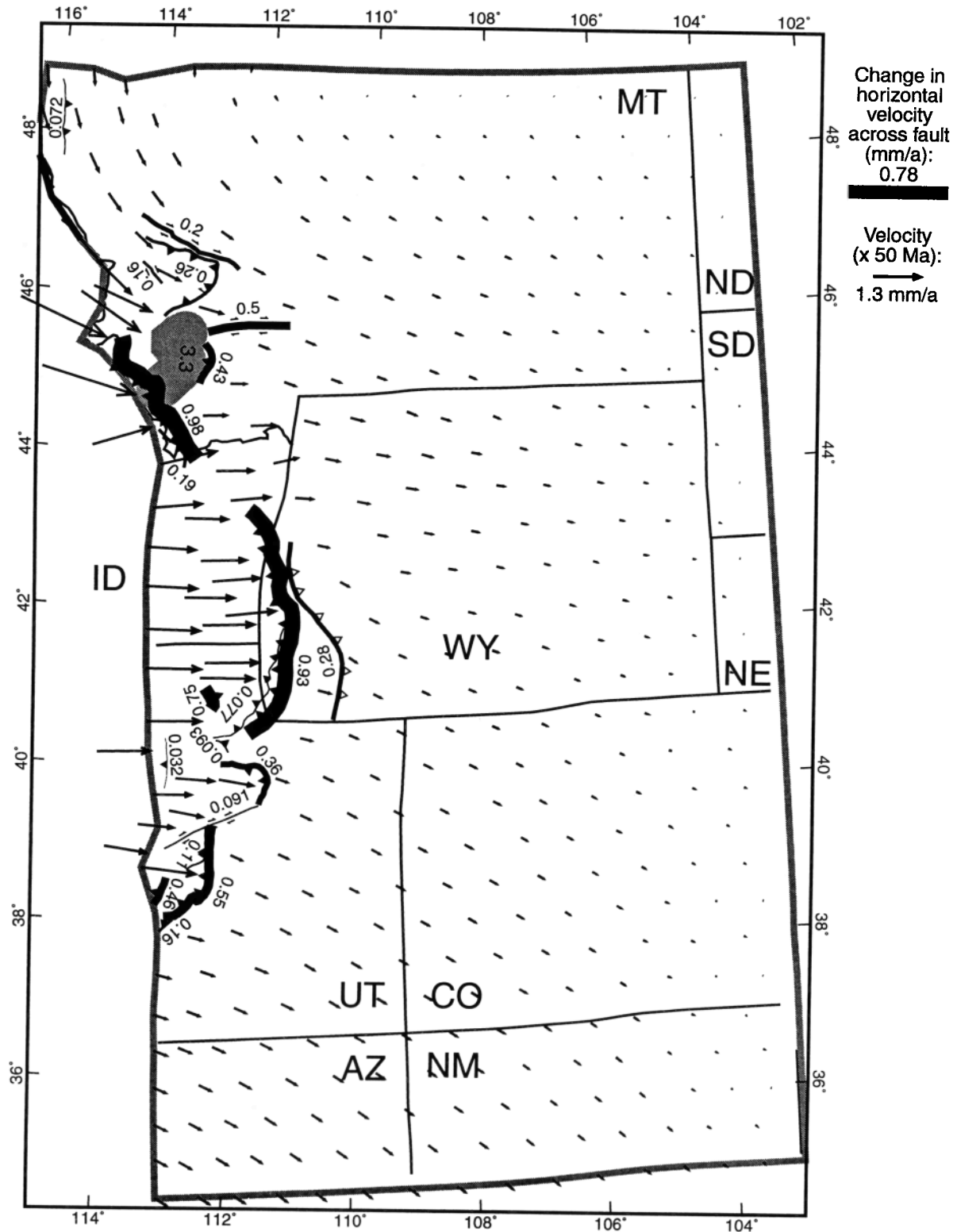


**Figure 3.** Paleotectonics during 80-75 Ma (Late Cretaceous: Campanian). Velocity vectors are relative to eastern North America. (Note that velocities are multiplied by 50 Ma, not 5 Ma, for legibility.) Width of fault traces is proportional to the magnitude of the horizontal component of the velocity change across the fault, and traces are labeled with this velocity change in  $\text{mm yr}^{-1}$ . (The fast moving Pioneer-Kelly-Grasshopper thrust in Montana is shown shaded to improve legibility.) State lines and grid outline are restored; latitude and longitude ticks in the margin show the undeformed reference frame of eastern North America. At this time, the only activity is the Sevier orogeny in the Overthrust Belt.



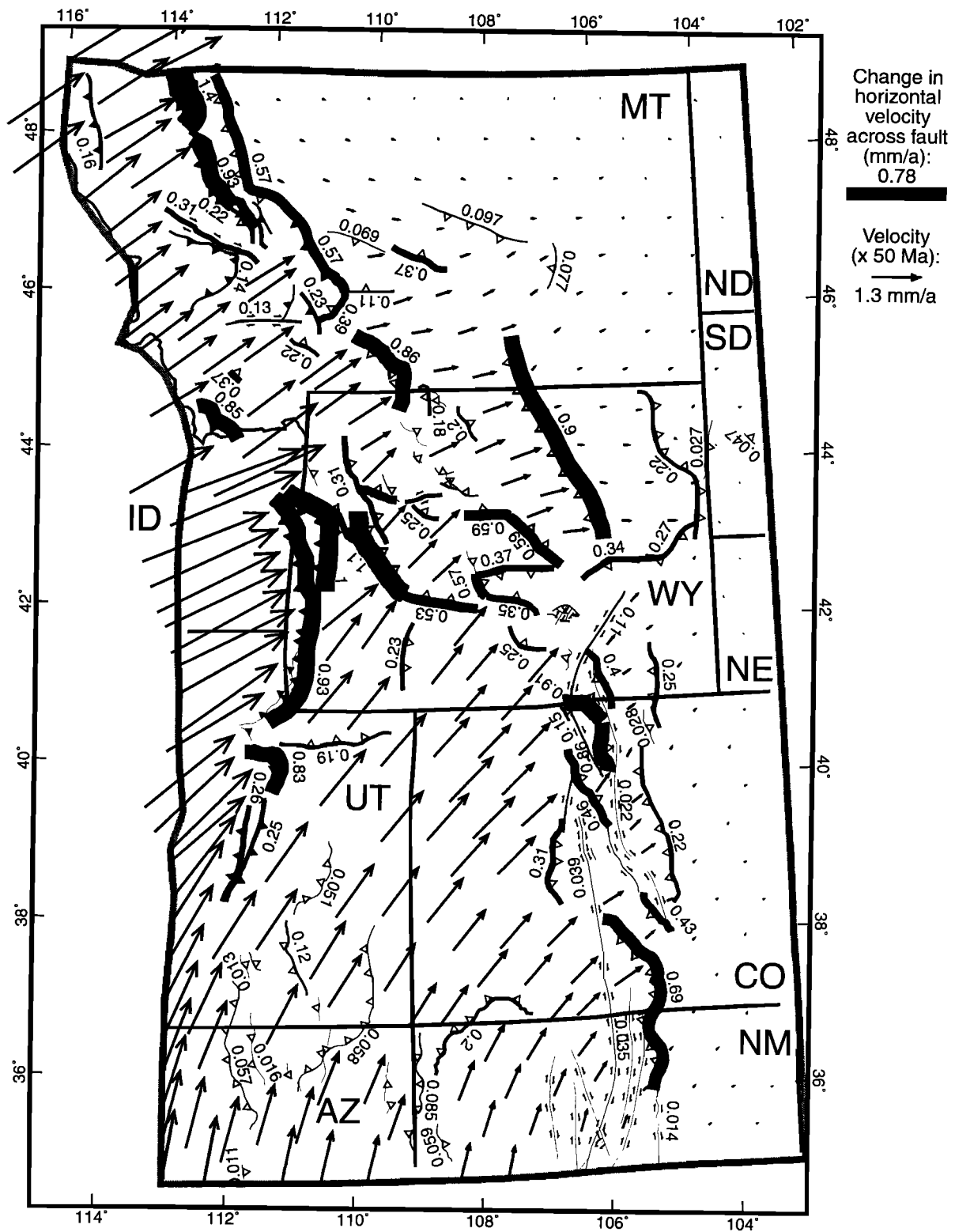


**Figure 5.** Paleotectonics at 60-55 Ma (late Paleocene-early Eocene). Conventions are as in Figure 3. This is the time of highest mean velocity in the Rocky Mountain foreland and Colorado Plateau. Laramide shortening in all regions (eastward to the Black Hills of South Dakota) was simultaneous with late Sevier orogeny in the western parts of the region. Note the rotational component of the motion of the Colorado Plateau.

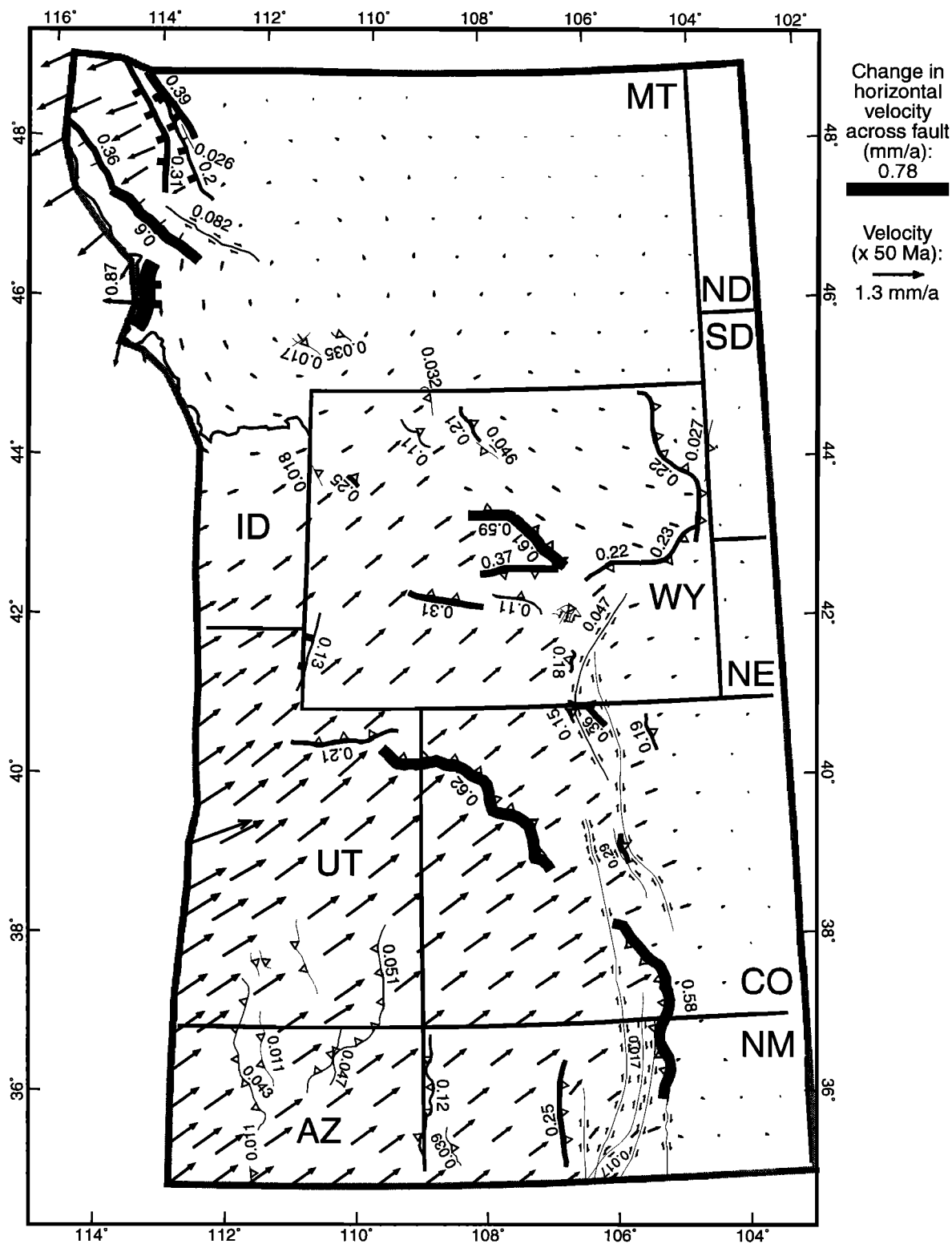


**Figure 6.** Paleotectonics during 45-40 Ma (middle Eocene). Conventions are as in Figure 3. The Sevier orogeny is over. Foreland velocities are only half as large as in Figure 5, and velocity vectors have rotated clockwise about 15°. The late Laramide structures are generally those farthest to the east and south. Note the beginning of extension in northwest Montana.



Hamilton [1981], who estimated the rotation as  $2^{\circ}$ - $4^{\circ}$  during the Laramide orogeny alone, with a very similar pole position.

This net rotation result may help to resolve the controversy that has grown up about the interpretation of paleomagnetic data from the Colorado Plateau. Originally, Steiner [1986] found post-Triassic clockwise rotation of  $11^{\circ} \pm 4^{\circ}$  and attributed the excess over Hamilton's figure to post-Laramide rotation. Bryan and Gordon [1990] interpreted all available Jurassic and earlier data as showing less post-Jurassic clockwise rotation:  $5.0^{\circ} \pm 2.4^{\circ}$ . Bazard and Butler [1991] reviewed the literature and preferred values of  $3.5^{\circ}$ - $6.3^{\circ}$ . However, Kent and Witte [1992] reopened the controversy by amending the North America polar wander path to one that implies Colorado Plateau rotation of  $13.5^{\circ} \pm 3.5^{\circ}$ . Molina Garza et al. [1998] responded with a calculation showing only  $5.1^{\circ} \pm 3.8^{\circ}$  of rotation when data from the Triassic rift basins of eastern North America are excluded.

This new result ( $3^{\circ}$ ) is largely independent of the data quoted in these papers, since my method is only able to use

sites where the rocks have been magnetized during the time span of the computation (0-85 Ma), and there are only four such sites on the Colorado Plateau (none with statistically significant rotations). It is also probably more precise than any of the paleomagnetic studies since it is based primarily on net fault offsets, which have mostly been measured to precisions of 1 km or better. (It is true that converting some fault throws to fault heaves requires the assumption of fault dip; however, in order to increase this rotation result by a factor of 2, it would be necessary to change the assumed dip of thrusts from  $25^{\circ}$  to  $13^{\circ}$ , which is implausible for an average dip of all Laramide thrusts throughout the brittle upper crust.)

In the rest of the computed history, rotation is minimal. The velocity field of the Rocky Mountain foreland is simple enough in most time steps to be reasonably described by a mean azimuth and a mean velocity, and this is done in Figures 7 (azimuth history) and 8 (velocity history). The mean azimuth is computed by summing the velocity components  $v$  (southward) and  $w$  (eastward) separately over all nodes of the Colorado Plateau, Rocky Mountain foreland, and Great

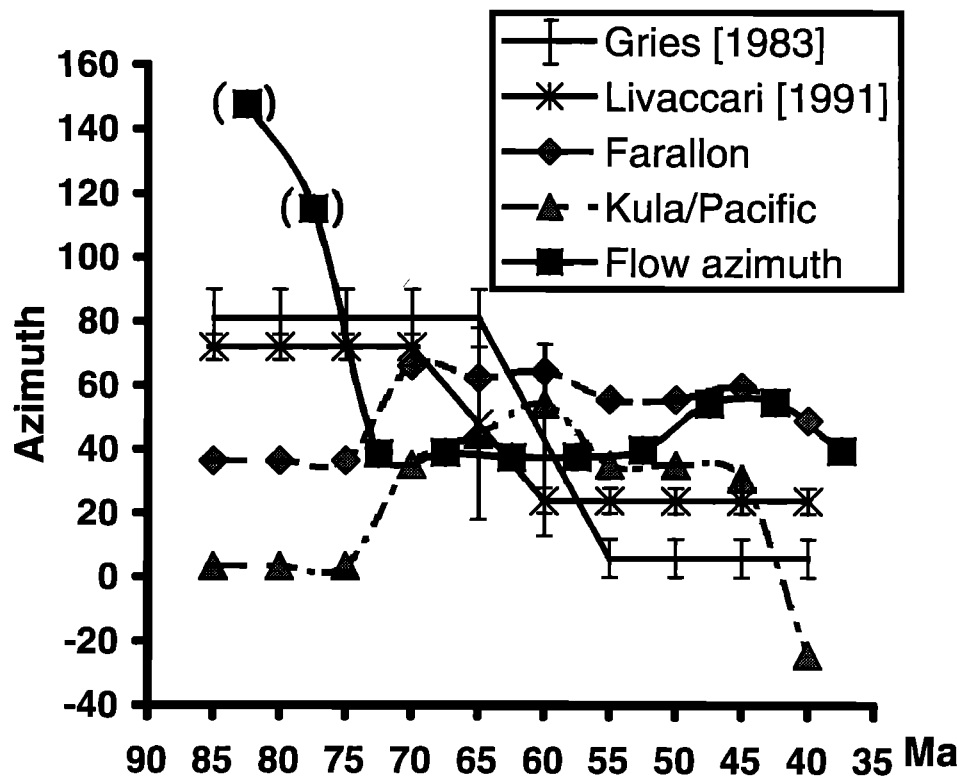
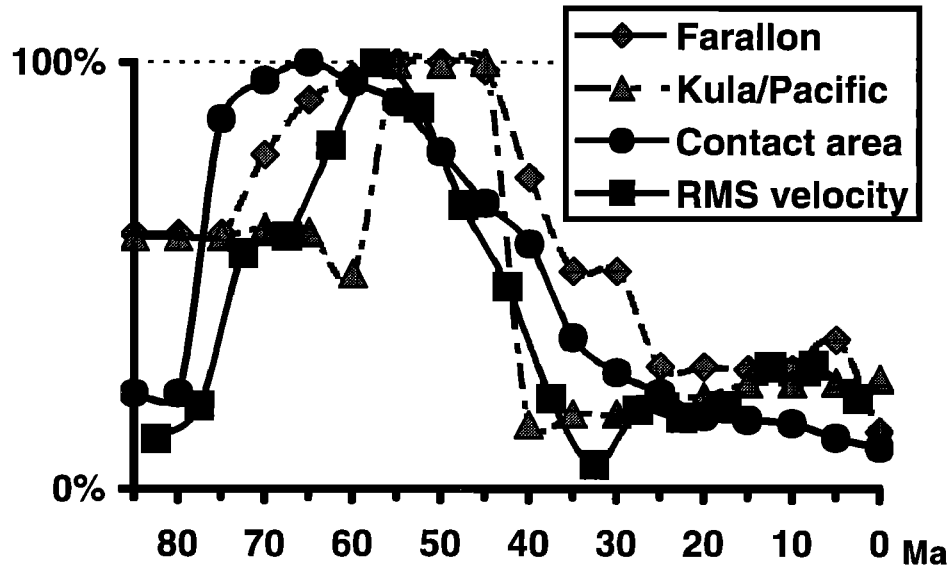


Figure 7. Computed history of the mean azimuth of crustal flow in the Rocky Mountain Foreland and Colorado Plateau (squares), compared to the azimuth histories expected for possible causes. (Crustal flow azimuths are in parentheses until 75 Ma because velocities are very low and these azimuths are probably not reliable.) Curves labeled "Farallon" and "Kula/Pacific" are the azimuths of the velocities of those plates with respect to stable North America at ( $38^{\circ}$ N,  $109^{\circ}$ W) according to stage poles from Engebretson et al. [1985]. Curve labeled "Gries [1983]" shows the inferred history of shortening direction that she attributed to changes in the direction of the absolute velocity of North America. Curve labeled "Livaccari [1991]" shows the inferred history of shortening direction that he attributed to the rise and fall of segments of the western cordillera. No model is satisfactory for all times. Probably the shortening direction was controlled by slip partitioning and slumping of the cordillera before 75 Ma (early Sevier orogeny) but was then controlled by coupling to one or both subducted oceanic plates during 75-35 Ma (Laramide orogeny). There is a suggestion that azimuth was controlled by the Kula plate before 50 Ma and by the Farallon plate after 50 Ma.



**Figure 8.** Computed history of the RMS velocity of crustal flow in the Rocky Mountain Foreland and Colorado Plateau (squares), compared to the histories of the magnitudes of possible causes. All curves are normalized to a maximum of 100%. The maximum of RMS velocity was  $1.06 \text{ mm yr}^{-1}$ . Curves labeled “Farallon” and “Kula/Pacific” are the velocity histories of those plates with respect to eastern North America; their maxima were  $155$  and  $190 \text{ mm yr}^{-1}$ , respectively. Curve labeled “contact area” is the inferred area of contact between North America and subducted oceanic slab(s), in the latitude range of the United States, with maximum  $1.85 \times 10^6 \text{ km}^2$ , according to Figure 31 of Bird [1992] which was derived from volcanic-arc positions mapped by Dickinson and Snyder [1978] and slab window areas from Dickinson and Snyder [1979]. The area of contact is the best predictor of the rate of Laramide deformation, especially if they were linked by a power law relationship.

Plains (but not the Sevier belt). I then define the mean azimuth as  $\langle \gamma \rangle \equiv \text{ATAN2}(\sum w_x, -\sum w_y)$ , where ATAN2 is the two-argument inverse tangent of Fortran. Since the eastern edge of the model is fixed, the mean velocity azimuth is also the mean shortening direction. The mean foreland velocity is the root-mean-square (RMS) value across the same area (the whole model region, except the Sevier belt).

These histories are important new information which can be used to choose among the models that have been proposed for the driving mechanism of the Laramide orogeny. At least five different concepts have been proposed in the literature: (1) Laramide compression was parallel to the absolute motion of North America [Gries, 1983]; (2) the Laramide orogeny was caused by the subduction of an oceanic plateau under North America [Livaccari *et al.*, 1981; Henderson *et al.*, 1984]; (3) the orogeny was caused by the accretion of the “Baja British Columbia” superterrane and its subsequent northward drift [Maxson and Tikoff, 1996]; (4) the driving force was transmitted from subduction zones on the western margin, mediated by a hot mobile cordillera [Livaccari, 1991]; or (5) the orogeny was caused by the basal drag of horizontally subducting oceanic plates [Dickinson and Snyder, 1978; Bird, 1988].

Gries’ [1983] concept was based on a pattern inferred from a regional synthesis: that shortening until 65 Ma was along azimuths of  $72^\circ$ - $90^\circ$ , while shortening during 55-40 Ma was along azimuths of  $0^\circ$ - $12^\circ$ . During the transition, a rapid counterclockwise rotation of stress was inferred. This history was explained as a result of the change in absolute motion of North America from westward to southward. My results (Fig-

ure 7) do not show any counterclockwise rotation after the beginning of the Laramide at 75 Ma; in fact, there is a  $15^\circ$  clockwise rotation at about 50 Ma. The profound difference between our results stems from the different age ranges that we assigned to individual structures; using more complete data, Dickinson *et al.* [1988] also found that some of Gries’ age assignments were in need of revision.

The subduction of an oceanic plateau [Livaccari *et al.*, 1981; Henderson *et al.*, 1984] may have occurred, but it cannot be the sole cause of the Laramide orogeny because the duration of the orogeny was too great. As these results show, continuous orogeny persisted at least from 75 until 40-35 Ma. During this time, any feature attached to the Farallon plate or the Kula plate moved about 4900 km with respect to North America. In contrast, the distance from the continental margin (former trench) to the Black Hills was probably no more than the present distance of 1550 km. Therefore the hypothetical plateau could not have remained long enough in a position where it could apply compression to the foreland. If subduction of an oceanic plateau occurred, it might have been an indirect cause of the orogeny by initiating a period of horizontal subduction (discussed below).

A related idea was presented by Maxson and Tikoff [1996]: the Laramide orogeny was due to lateral forces from the accretion and northward drift of the “Baja British Columbia” superterrane on the western margin of North America. They did not explain why these events should affect the stress state of the continental interior. However, one might reasonably expect the greatest stress pulse at the time of initial accretion, at 94 Ma, and one might expect it to radiate from the region

of accretion in present northern Mexico. However, my results show that NE directed shortening occurred strictly after 75 Ma. Furthermore, there was no steady and systematic rotation of shortening directions, as one would expect if the source of the stress were moving northward from Mexico to Canada during 94-40 Ma. Therefore the accretion and motion of "Baja British Columbia" may have occurred, but they were not the causes of the Laramide orogeny.

Like *Gries* [1983], *Livaccari* [1991] inferred a rapid change in shortening direction during the Laramide orogeny, from azimuths of 68°-76° before 65 Ma to azimuths of 20°-28° afterward. *Livaccari* interpreted the pattern he saw as the result of successive collapse of first the northern and then the southern parts of a western cordillera with an elevated, weak, extending core. Thus he was extending the mechanical ideas of *Burchfiel and Davis* [1975]. Actually, any model in which the lateral force for the Laramide orogeny is transmitted through a high, weak cordillera is also implicitly a model in which this force is generated by North America/Farallon or North America/Kula coupling in a coastal subduction zone. (If it were not, the cordillera would be unconfined on the west and would collapse rapidly in an enormous landslide.) Fortunately, while the elevation history of the cordillera is elusive and debatable, the history of relative plate motions with respect to North America is known [e.g., *Jurdy*, 1984; *Engelbreton et al.*, 1985]. If we temporarily postpone consideration of horizontal subduction, the other most plausible reasons for increased transmission of horizontal compression across the subduction zone would be a decrease in trench depth or an increase in viscous shear coupling. The first factor was undoubtedly present, since the ages of the parts of the reconstructed oceanic plates that were entering the trench became gradually less throughout the Tertiary. However, this younging was continuous, and it is difficult to see how it could have given rise to an orogeny with a well-defined beginning and end. Therefore, in this class of models it is necessary to appeal to increased viscous shear stress transmission across the subduction thrust, probably caused by increased relative plate velocity. Comparing the normalized velocity histories from *Engelbreton et al.* [1985] in Figure 8, we see that increased Farallon/North America velocity at 70 Ma comes a little too late to explain the beginning of the Laramide orogeny, and increased Kula/North America velocity comes 20 m.y. too late. There is also a problem about the end of the Laramide, since both Farallon and Kula velocities with respect to North America peaked at 55-45 Ma, a time when the orogeny was waning. Using a different plate reconstruction scheme (imposing Antarctic deformation and ignoring hotspots), *Jurdy* [1984] proposed a slightly different history of Farallon/North America relative velocities. This alternate velocity history has velocities exceeding 100 mm yr<sup>-1</sup> only at 60 Ma and peaking at 50 Ma. Thus it also peaks too late to correlate well with my history of velocity.

The remaining proposal is that the Laramide orogeny was caused by increased shear coupling between North America and the Farallon and/or Kula plate(s) caused by increased contact area during an episode of horizontal subduction. Horizontal subduction was originally invoked to explain the inland migration of the volcanic arc [*Snyder et al.*, 1976; *Dickinson and Snyder*, 1978], and this gives an independent

basis for estimating the changing area of contact. The curve shown in Figure 8 is computed from Figure 31 of *Bird* [1992], which, in turn, was based on Figures 3-5 of *Dickinson and Snyder* [1978]. It shows that contact area probably increased by a factor of 4 very rapidly during 80-75 Ma and that the area remained large until 55 Ma and declined continuously thereafter. Of the curves considered, this is the best match to the velocity history computed in this paper. It is true that the velocity history is more strongly peaked than the history of contact area. However, this is an expected consequence of the nonlinear rheology of continental lithosphere. If total horizontal force transmission was proportional to contact area, then all velocities and strain rates within North America would be expected to be proportional to some power of the contact area.

The directions of foreland velocity and shortening (Figure 7) are also reasonably consistent with the directions of oceanic plate motion after 75 Ma. (Of course, there are possible circumstances, such as anisotropy and heterogeneity, which could cause the surface velocity to diverge from the direction of basal drag, so this coincidence is not proof.) The foreland velocity and shortening azimuth of 40° that was maintained during 75-50 Ma is very close to the predicted azimuth of Kula plate motion. During 50-35 Ma, however, the azimuth of foreland velocity better matches the azimuth of the Farallon plate. There is a model already published that (implicitly) makes a similar prediction: *Engelbreton et al.* [1985] attempted to explain northward transport of coastal terranes by their "southern option" model, in which the Kula plate was subducting beneath the United States from 85-59 Ma. During 59-45 Ma (in their model), a long Kula-Farallon transform was subducted at the coast and moved gradually under the Rocky Mountains, changing the identity and azimuth of the flat slab from Kula to Farallon (Figure 9). The transition in velocity azimuth that I see around 50 Ma is an excellent match to their suggestion.

In conclusion, the best explanation for Cretaceous-Tertiary orogenies in the western United States seems to be a composite one. In the early Sevier orogeny (before 75 Ma), driving force was transmitted through a weak, elevated cordillera, as argued by *Burchfiel and Davis* [1975] and *Livaccari* [1991]. Perhaps coast-parallel shear components were absorbed in coastal strike-slip systems and cordilleran deformation [e.g., *Tikoff and de Saint Blanquat*, 1997], and only normal stresses perpendicular to the cordillera were transmitted inland (Figure 9). However, the Laramide orogeny was a distinct and different event, during which the bulk of the driving force was applied to the base of North America by horizontally subducting slabs of oceanic lithosphere. Consequently, the azimuth of shortening was controlled by the azimuth of relative plate motion, while the rate of shortening was controlled by the changing area of contact between plates. More tentatively, it appears that the change in stress directions that occurred around 50 Ma may have marked the passage of an active Kula-Farallon transform within the horizontal subducting slabs.

#### 4. Conclusions

A new paleotectonic and palinspastic method was applied to the Rocky Mountain foreland region, using reasonably

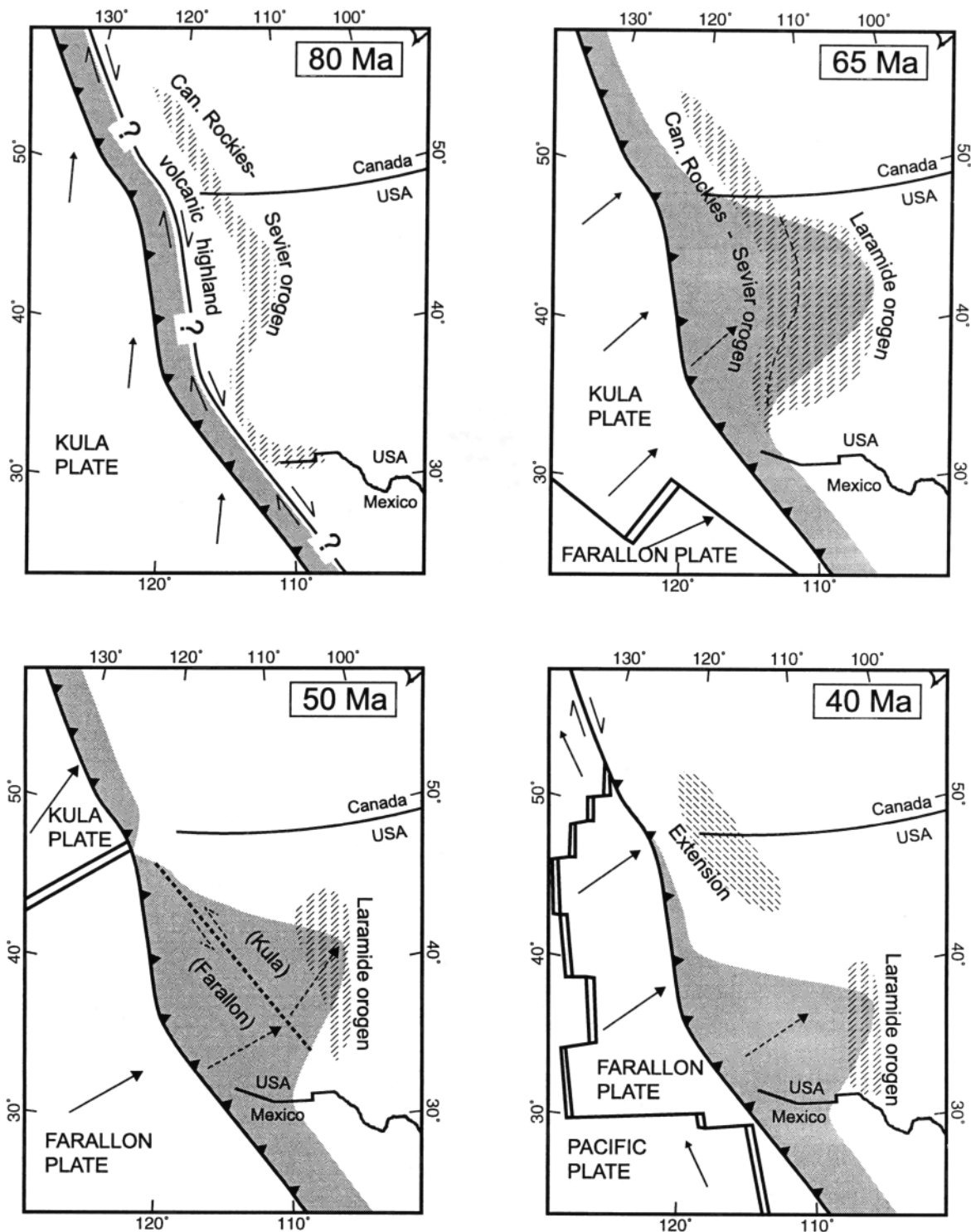


**Figure 9.** Proposed history of plate configurations based on this study, on plate reconstructions of *Engebretson et al.* [1985], and on volcanic arc fronts from *Dickinson and Snyder* [1978] and *Urrutia-Fucugauchi* [1986]. Shading shows the forearc area of contact between the base of North America and the tops of subducting slabs. Diagonal pattern shows regions of orogeny or extension. At 80 Ma, oblique subduction of the Kula plate caused partitioned deformation: coastal terranes moved north, while the volcanic highland transmitted only eastward pressure to the Canadian Rocky Mountains and Sevier orogen. By 65 Ma, horizontal subduction under a huge area drove the Laramide orogeny (and the continuing Canadian Rocky Mountains-Sevier orogeny). About 50 Ma, a subducted Kula/Farallon transform boundary may have passed under the forearc, changing the direction of basal tractions. The last stage of the Laramide orogeny, around 40 Ma, was driven by horizontal subduction of the Farallon slab in the southwestern United States and northwest Mexico.

complete data from the literature through publication year 1997. Velocities, strain rates, and fault-slip histories were computed back to 85 Ma in 5 m.y. time steps. As expected, the solution displays the last stages of the Sevier orogeny during 85-50 Ma, the Laramide orogeny during 75-35 Ma, and Neogene extension spreading southward after 50 Ma. The solution also provides estimated slip histories of each fault during each event; 64% of these are different from the simple constant-rate histories that were assumed at the beginning of the computation. However, the most interesting result is the estimate of the horizontal velocity field over time.

Foreland velocities peaked at 1.5 mm yr<sup>-1</sup> during 60-55 Ma, when the Colorado Plateau was rotating clockwise around an Euler pole in the northern part of Texas, as predicted by *Hamilton* [1981]. The computed total rotation of the plateau about a vertical axis since 85 Ma is only 3°, which is less than claimed by some authors working with paleomagnetic poles of older rocks but is the same as the lower limit quoted by *Bryan and Gordon* [1990].

During the Laramide orogeny in the foreland, the mean shortening azimuth was steady at 40° until 50 Ma and then rotated clockwise to 55°; the counterclockwise stress rotation proposed by *Gries* [1983] and by *Livaccari* [1991] did not occur. The mean velocity directions (with respect to eastern North America) are similar to the known relative velocities of the Kula and Farallon plates, which were subducting beneath North America. However, the history of velocity and strain rate magnitudes does not match well with the histories of the relative velocities of these oceanic plates. Instead, the rates of Laramide deformation were more closely related to the changing area of contact between North America and the oceanic plates, confirming that the most likely driving mechanism for the orogeny was the transmission of basal shear stress during an episode of horizontal subduction.

## Appendix A: Algorithm

### A1. Least Squares Formalism

I assume that all geologic and paleomagnetic data that constrain displacement, strain, and/or rotation in a particular time step have been transformed to scalar rate estimates  $r_k^n$ . (The subscript  $k = 1, \dots, K$  identifies the datum, and the superscript  $n$  identifies the time step.) Let the corresponding scalar rate predictions derived from the velocity field of the finite element model in a particular timestep be called  $p_k^n$ . (In the remainder of this section, I will discuss only a single computational time step, so the superscript  $n$  will be suppressed.) I further assume that each scalar rate  $r_k$  has an uncertainty that can be approximated by a Gaussian probability distribution with standard deviation  $\sigma_k$  and that the errors in these rates are independent. (A Gaussian probability distribution is reasonably appropriate for the numerator in each rate, which is an amount of strain or displacement. It is not appropriate for the denominator, the elapsed time, which typically comes with a hard upper limit based on cross-cutting relations but without any lower limit. Because of this, I will iterate the solution of the entire history in a way that allows additional degrees of freedom in each rate history; this method is described below. However, in each individual it-

eration, the elapsed time is held constant, giving a Gaussian distribution for the rate.)

Finally, I assume that there is a probability  $0 \leq q_k \leq 1$  that each datum is relevant to the time step. Normally,  $q_k$  is unity because irrelevant data are simply omitted from the list  $k = 1, \dots, K$ . However, in the cases of certain paleostress data, fractional  $q_k$  are required. The natural logarithm of the density of the joint probability that the velocity model matches all the relevant rates is then formed from the individual probability densities ( $\Phi$ ) as

$$S \equiv \ln \left\{ \prod_{k=1}^K [\Phi(p_k = r_k)]^{q_k} \right\} = \sum_{k=1}^K q_k \ln [\Phi(p_k = r_k)] = - \sum_{k=1}^K q_k \left[ \frac{(p_k - r_k)^2}{2\sigma_k^2} + \ln(\sigma_k) + \ln\sqrt{2\pi} \right]. \quad (1)$$

I refer to this quantity  $S$  as the “score” of the velocity solution, which is to be maximized. That is, the sum of squares of the relevant prediction errors (each divided by the variance of the corresponding rate) is to be minimized.

On the surface of a spherical planet with radius  $R$ , I define a coordinate system of colatitude ( $\theta$ ) measured southward from the north pole and longitude ( $\phi$ ) measured eastward from the prime meridian. The unknowns in each velocity solution are the horizontal  $\theta$  components and  $\phi$  components of the velocity of the surface. The predicted rates  $p_k$  can be expressed as a linear combination of the velocity components  $v$  (southward) and  $w$  (eastward) at each of the  $J$  nodes of a finite element grid:

$$p_k = c_k + \sum_{j=1}^J (f_{kj}v_j + g_{kj}w_j) \quad (2)$$

With this linear relation,  $S$  is a quadratic form in the nodal-velocity-component values  $v_j$  and  $w_j$ , so it is maximized by finding the single stationary point in multi dimensional velocity space where

$$\frac{\partial S}{\partial v_i} = 0 = \frac{\partial S}{\partial w_i}; \quad i = 1, \dots, J. \quad (3)$$

Algebraically, this leads to a  $2J \times 2J$  linear system, which can be thought of as being partitioned into four submatrices times two subvectors equaling two subvectors:

$$\begin{bmatrix} A_{ij} & B_{ij} \\ C_{ij} & D_{ij} \end{bmatrix} \begin{bmatrix} v_j \\ w_j \end{bmatrix} = \begin{bmatrix} E_i \\ F_i \end{bmatrix} \quad (4)$$

using the abbreviations

$$A_{ij} = \sum_{k=1}^K \frac{f_{ki}f_{kj}}{\sigma_k^2} \quad B_{ij} = \sum_{k=1}^K \frac{f_{ki}g_{kj}}{\sigma_k^2} \quad (5)$$

$$C_{ij} = \sum_{k=1}^K \frac{g_{ki}f_{kj}}{\sigma_k^2} \quad D_{ij} = \sum_{k=1}^K \frac{g_{ki}g_{kj}}{\sigma_k^2}$$

$$E_i = \sum_{k=1}^K \frac{f_{ki}(r_k - c_k)}{\sigma_k^2} \quad (6)$$

$$F_i = \sum_{k=1}^K \frac{g_{ki}(r_k - c_k)}{\sigma_k^2}$$

**A2. Boundary Conditions**

The equations stated above are singular in the absence of boundary conditions. Some edge(s) of the model must be fixed (or moved in a predetermined way) to provide a velocity reference frame. I replace the row equations that state that  $S$  is stationary with respect to variations in these nodal velocity components with simpler equations stating the desired values of these components.

This method permits only velocity boundary conditions not stress boundary conditions. Along each axis ( $\theta$  or  $\phi$ ), one boundary should be constrained and one left free (because integrating strain information to find velocities is like solving first-order differential equations). When one margin of a continent is facing a subduction zone, it is best to leave that boundary free.

**A3. A Priori or Pseudo Data**

An essential context for all the geologic data showing locally intense straining is that they should be overlaid on a set of a priori data (or "pseudo data") stating that in other places the strain rate is close to zero. An appropriate formalism is to assign a zero target strain rate, with a statistical uncertainty. A larger standard deviation should be attached to this null hypothesis in complex regions where unknown faults and orogenic phases might have been buried or overlooked.

To implement these constraints, the score  $S$  of any velocity solution, which is to be optimized, is first augmented by a term

$$\Delta S = -W \iint_U \frac{\dot{\epsilon}_{\theta\theta}^2 + \dot{\epsilon}_{\theta\phi}^2 + \dot{\epsilon}_{\phi\phi}^2 + \dot{\epsilon}_{\phi\theta}^2}{\mu^2} dU \quad (7)$$

where  $W$  is the weight coefficient for all pseudo data (in units of  $m^{-2}$ ),  $\mu$  is the standard deviation of the (nominally zero) strain rate (per second), and  $U$  is the area without active faults. In practice, any finite element that has no active fault crossing it is a part of  $U$ . Weighting by area is used to make this new term roughly independent of local variations in finite element size. However, an appropriate value for the weight coefficient  $W$  is approximately the inverse of the mean of the areas of all finite elements, as explained below.

This term has the effect of causing unfaulted areas to behave as Newtonian viscous sheets of lithosphere. The algorithm will adjust the velocity in each time step to minimize the area integral of squared strain rates for these elements; this is exactly the result one obtains by beginning from the momentum equation (in the absence of horizontal forces), adopting a linear rheology, and solving for velocity with inhomogeneous boundary conditions.

The  $2 \times 2$  strain rate tensor  $\tilde{\epsilon}$  on the spherical surface is calculated by summing spatial derivatives of the nodal functions. The nodal functions that I use were introduced by Kong and Bird [1995] and shown to satisfy the requirements of horizontality, continuity, and completeness:

$$\begin{bmatrix} v(\theta, \phi) \\ w(\theta, \phi) \end{bmatrix} = \sum_{j=1}^J \begin{bmatrix} G_{1,1}^j(\theta, \phi) & G_{2,1}^j(\theta, \phi) \\ G_{1,2}^j(\theta, \phi) & G_{2,2}^j(\theta, \phi) \end{bmatrix} \begin{bmatrix} v_j \\ w_j \end{bmatrix}. \quad (8)$$

In this notation, the superscript  $j$  on the vector nodal function  $\vec{G}_x^j$  or nodal function component  $G_{x,y}^j$  identifies the node that has unit velocity (all other nodes having zero velocity in this particular nodal function). Subscript  $x=1$  indicates the nodal function associated with unit southward velocity  $v$ ; subscript  $x=2$  indicates the nodal function associated with unit eastward velocity  $w$ . Subscript  $y=1$  indicates the southward or  $\theta$  component of the vector nodal function  $\vec{G}_x^j$ , and subscript  $y=2$  indicates the eastward or  $\phi$  component.

The coefficients of the linear system are augmented by

$$\begin{aligned} \Delta A_{\ell} &= \frac{W}{R^2} \sum_{\ell=1}^L \frac{1}{\mu_{\ell}^2} \iint_{a_{\ell}} \left[ \begin{aligned} &2 \frac{\partial G_{1,1}^{\ell}}{\partial \theta} \frac{\partial G_{1,1}^{\ell}}{\partial \phi} + \csc \theta \left( \frac{\partial G_{1,1}^{\ell}}{\partial \theta} \frac{\partial G_{1,2}^{\ell}}{\partial \phi} + \frac{\partial G_{1,2}^{\ell}}{\partial \theta} \frac{\partial G_{1,1}^{\ell}}{\partial \phi} \right) + \\ &\cot \theta \left( \frac{\partial G_{1,1}^{\ell}}{\partial \theta} G_{1,1}^{\ell} + G_{1,1}^{\ell} \frac{\partial G_{1,1}^{\ell}}{\partial \theta} \right) + \\ &2 \left( \csc \theta \frac{\partial G_{1,2}^{\ell}}{\partial \phi} + \frac{G_{1,1}^{\ell}}{\tan \theta} \right) \left( \csc \theta \frac{\partial G_{1,2}^{\ell}}{\partial \phi} + \frac{G_{1,1}^{\ell}}{\tan \theta} \right) + \\ &\frac{1}{2} \left( \csc \theta \frac{\partial G_{1,1}^{\ell}}{\partial \phi} + \frac{\partial G_{1,2}^{\ell}}{\partial \theta} - \frac{G_{1,2}^{\ell}}{\tan \theta} \right) \left( \csc \theta \frac{\partial G_{1,1}^{\ell}}{\partial \phi} + \frac{\partial G_{1,2}^{\ell}}{\partial \theta} - \frac{G_{1,2}^{\ell}}{\tan \theta} \right) \end{aligned} \right] da_{\ell} \\ \Delta B_{\ell} &= \frac{W}{R^2} \sum_{\ell=1}^L \frac{1}{\mu_{\ell}^2} \iint_{a_{\ell}} \left[ \begin{aligned} &2 \frac{\partial G_{2,1}^{\ell}}{\partial \theta} \frac{\partial G_{2,1}^{\ell}}{\partial \phi} + \csc \theta \left( \frac{\partial G_{2,1}^{\ell}}{\partial \theta} \frac{\partial G_{2,2}^{\ell}}{\partial \phi} + \frac{\partial G_{2,2}^{\ell}}{\partial \theta} \frac{\partial G_{2,1}^{\ell}}{\partial \phi} \right) + \\ &\cot \theta \left( \frac{\partial G_{2,1}^{\ell}}{\partial \theta} G_{2,1}^{\ell} + G_{2,1}^{\ell} \frac{\partial G_{2,1}^{\ell}}{\partial \theta} \right) + \\ &2 \left( \csc \theta \frac{\partial G_{2,2}^{\ell}}{\partial \phi} + \frac{G_{2,1}^{\ell}}{\tan \theta} \right) \left( \csc \theta \frac{\partial G_{2,2}^{\ell}}{\partial \phi} + \frac{G_{2,1}^{\ell}}{\tan \theta} \right) + \\ &\frac{1}{2} \left( \csc \theta \frac{\partial G_{2,1}^{\ell}}{\partial \phi} + \frac{\partial G_{2,2}^{\ell}}{\partial \theta} - \frac{G_{2,2}^{\ell}}{\tan \theta} \right) \left( \csc \theta \frac{\partial G_{2,1}^{\ell}}{\partial \phi} + \frac{\partial G_{2,2}^{\ell}}{\partial \theta} - \frac{G_{2,2}^{\ell}}{\tan \theta} \right) \end{aligned} \right] da_{\ell} \\ \Delta D_{\ell} &= \frac{W}{R^2} \sum_{\ell=1}^L \frac{1}{\mu_{\ell}^2} \iint_{a_{\ell}} \left[ \begin{aligned} &2 \frac{\partial G_{2,1}^{\ell}}{\partial \theta} \frac{\partial G_{2,1}^{\ell}}{\partial \phi} + \csc \theta \left( \frac{\partial G_{2,1}^{\ell}}{\partial \theta} \frac{\partial G_{2,2}^{\ell}}{\partial \phi} + \frac{\partial G_{2,2}^{\ell}}{\partial \theta} \frac{\partial G_{2,1}^{\ell}}{\partial \phi} \right) + \\ &\cot \theta \left( \frac{\partial G_{2,1}^{\ell}}{\partial \theta} G_{2,1}^{\ell} + G_{2,1}^{\ell} \frac{\partial G_{2,1}^{\ell}}{\partial \theta} \right) + \\ &2 \left( \csc \theta \frac{\partial G_{2,2}^{\ell}}{\partial \phi} + \frac{G_{2,1}^{\ell}}{\tan \theta} \right) \left( \csc \theta \frac{\partial G_{2,2}^{\ell}}{\partial \phi} + \frac{G_{2,1}^{\ell}}{\tan \theta} \right) + \\ &\frac{1}{2} \left( \csc \theta \frac{\partial G_{2,1}^{\ell}}{\partial \phi} + \frac{\partial G_{2,2}^{\ell}}{\partial \theta} - \frac{G_{2,2}^{\ell}}{\tan \theta} \right) \left( \csc \theta \frac{\partial G_{2,1}^{\ell}}{\partial \phi} + \frac{\partial G_{2,2}^{\ell}}{\partial \theta} - \frac{G_{2,2}^{\ell}}{\tan \theta} \right) \end{aligned} \right] da_{\ell} \end{aligned} \quad (9)$$

where  $\ell = 1, \dots, L$  identifies the "nonfaulting" elements comprising  $U$ , with individual areas  $a_{\ell}$ . In practice, area integrals within each element are performed numerically, using seven Gauss points with associated weights [Zienkiewicz, 1971].

**A4. Use of Balanced Cross Sections**

Many structural geologists publish restored cross sections from which they estimate the amount of shortening or extension along the line of section. Dividing the amount of extension (compression is negative extension) by the time available gives the relative velocity component (along the line of section) for the endpoints, which is the rate estimate  $r_k$ . If the endpoints of the section are marked by position vectors  $b_k$  and  $d_k$ , then  $c_k = 0$  and

$$\begin{aligned}
f_{kj} &= G_{1,1}^j(\bar{b}_k) \cos \gamma(\bar{b}_k) - G_{1,1}^j(\bar{d}_k) \cos \gamma(\bar{d}_k) - \\
&G_{1,2}^j(\bar{b}_k) \sin \gamma(\bar{b}_k) + G_{1,2}^j(\bar{d}_k) \sin \gamma(\bar{d}_k) \\
g_{kj} &= G_{2,1}^j(\bar{b}_k) \cos \gamma(\bar{b}_k) - G_{2,1}^j(\bar{d}_k) \cos \gamma(\bar{d}_k) - \\
&G_{2,2}^j(\bar{b}_k) \sin \gamma(\bar{b}_k) + G_{2,2}^j(\bar{d}_k) \sin \gamma(\bar{d}_k)
\end{aligned} \quad (10)$$

where  $\gamma(b_k)$  and  $\gamma(d_k)$  are the forward azimuths at each end of the directed great circle arc  $b_k \rightarrow d_k$  (each measured clockwise from north).

#### A5. Use of Fault-Slip Data

A large fraction of the available data concern offsets on faults. While offset is actually a vector, I use only the larger of the dip-slip or strike-slip components and treat this as a scalar datum. This is because the strike-slip component of dominantly dip slip faults is rarely known, while any dip-slip on strike-slip faults is irrelevant to relative horizontal velocities. After division by the time available, this scalar offset becomes a scalar relative velocity component across the fault.

When a fault is long enough to cross several finite elements, I impose the same slip and slip rate in each element. In the case of rigid microplate tectonics, where each fault connects to other faults at triple junctions, this method is reasonably accurate. The other end-member is the case where no faults connect, but all terminate within the domain. In that case, each fault might be expected (on the basis of crack theory for linear materials) to have an ellipsoidal profile of slip versus length. Such "elliptical" faults would have a mean slip which is only 79% ( $\pi/4$ ) of their maximum slip. Thus my method might overstate strain by 27% in some cases where faults do not connect and where the geologic offsets reported are the maximum offsets. However, if the geologic offsets are considered to be determined at random points of convenience, then once again there is no systematic error.

If every fault extended continuously across the model from boundary to boundary, one could simply use its slip rate as a constraint on the relative velocity of the nodes on opposite sides of the fault. However, the number of faults in many applications is so great that such customized grids are prohibitively expensive to work with. Thus I have developed a more general approach, which allows any number of faults to cross a given finite element.

For each finite element, there are four steps: (1) Form the target strain rate tensor for that element as the sum of the strain rate tensors implied by all the active fault segments cutting that element; (2) Form the matrix of covariances of the strain rate components in that element as the sum of the covariances added by all the active fault segments, plus the small covariance of the strain rate in the continuum blocks between them; (3) Diagonalize the covariance matrix to find three principal axes (in strain rate space) along which the uncertainties are independent and also rotate the target strain rates into this new coordinate system; (4) Add these three independent targets as scalar data with known uncertainties in the global system of equations.

The strain rate tensor in the horizontal plane  $\tilde{\epsilon}$  is a second-rank tensor of size  $2 \times 2$ . I simplify the notation by treating the three independent components of the strain rate tensor

( $\dot{\epsilon}_{\theta\theta} = \dot{\epsilon}_{NS}, \dot{\epsilon}_{\theta\phi} = \dot{\epsilon}_{SE}, \dot{\epsilon}_{\phi\phi} = \dot{\epsilon}_{EW}$ ) as a one-subscript vector ( $\dot{\epsilon}_m; m = 1, 2, 3$ ), permitting me to write the covariance of strain rates as a  $3 \times 3$  matrix. If all the active fault segments that cut (even partway) through one finite element are numbered  $z = 1, \dots, Z$ , then I express the strain rate vector in the element as a linear combination of their scalar slip rates  $s_z$ :

$$\dot{\epsilon}_m = \sum_{z=1}^Z H_{zm} s_z; \quad m = 1, 2, 3. \quad (11)$$

The covariance matrix of the strain rate components is composed of two parts: the continuum compliance common to all parts of the lithosphere (see section A3) and the terms arising from the standard deviations  $\delta s_z$  of the scalar slip rates  $s_z$ :

$$\tilde{\nu} = \mu^2 \begin{bmatrix} 4/3 & 0 & -2/3 \\ 0 & 1 & 0 \\ -2/3 & 0 & 4/3 \end{bmatrix} + \sum_{z=1}^Z (\delta s_z)^2 \left[ \tilde{H}_z^T \tilde{H}_z \right] \quad (12)$$

To find  $H_z$  (the partial derivative of element strain rate with respect to slip rate of one active fault), I make the simplifying restriction that no node lies exactly on a fault. Also, I slightly straighten the traces of any fault segment that crosses the same element boundary more than once. Then, each fault segment (with its projected extensions, if necessary) must separate one node of the element from the other two. Let  $u_z$  be the index number of the isolated node. If node  $u_z$  is on the right side of the fault segment (when looking along its azimuth  $\gamma_z$ , measured clockwise from north), then I define the variable  $\eta_z$  as +1; otherwise, it is -1. Let  $\kappa_z$  be the fraction of the width of the element that is cut by the fault segment:  $0 < \kappa_z \leq 1$ .

In the case of a strike-slip fault, the scalar slip rate  $s_z$  is defined as the right-lateral offset divided by the time available. (Left-lateral offsets are negative right-lateral offsets.) Then

$$\tilde{H}_z = \frac{\eta_z \kappa_z}{R} \begin{pmatrix} \frac{\partial G_{1,1}^{u_z}}{\partial \theta} \cos \gamma_z - \frac{\partial G_{2,1}^{u_z}}{\partial \theta} \sin \gamma_z, \\ \frac{1}{2} \left( \frac{\partial G_{1,1}^{u_z}}{\partial \phi} \cos \gamma_z - \frac{\partial G_{2,1}^{u_z}}{\partial \phi} \sin \gamma_z + \frac{\partial G_{1,2}^{u_z}}{\partial \theta} \cos \gamma_z - \frac{\partial G_{2,2}^{u_z}}{\partial \theta} \sin \gamma_z - \frac{G_{1,2}^{u_z} \cos \gamma_z - G_{2,2}^{u_z} \sin \gamma_z}{\tan \theta} \right), \\ \frac{\partial G_{1,2}^{u_z}}{\partial \phi} \cos \gamma_z - \frac{\partial G_{2,2}^{u_z}}{\partial \phi} \sin \gamma_z + \frac{G_{1,1}^{u_z} \cos \gamma_z - G_{2,1}^{u_z} \sin \gamma_z}{\tan \theta} \end{pmatrix}, \quad (13a)$$

In the case of dip-slip faulting, it is most convenient to define  $s_z$  as the net horizontal extension perpendicular to the fault trace, divided by the time available. (Thrusting is considered to be negative extension.) In the case of detachment faulting, net horizontal extension is the distance from the breakaway fault in the footwall to the tip of the hanging wall (reconstructed if necessary), regardless of whether the fault slipped at a low angle or, alternatively, slipped at a high angle and then rotated during further extension. In the more common case of dip-slip faulting without horizontal-axis rotation of footwall or hanging wall, net horizontal extension is the rela-

tive vertical offset (throw) times the cotangent of the fault dip. My convention is that normal and detachment faulting have positive  $s_z$  and thrust faults have negative values. Then,

$$\bar{H}_z = \frac{\eta_z \kappa_z}{R} \left[ \begin{array}{c} \frac{\partial G_{1,1}^{u_z}}{\partial \theta} \sin \gamma_z + \frac{\partial G_{2,1}^{u_z}}{\partial \theta} \cos \gamma_z, \\ \frac{1}{2} \left( \frac{\partial G_{1,1}^{u_z}}{\partial \phi} \frac{\sin \gamma_z}{\sin \theta} + \frac{\partial G_{2,1}^{u_z}}{\partial \phi} \frac{\cos \gamma_z}{\sin \theta} + \frac{\partial G_{1,2}^{u_z}}{\partial \theta} \sin \gamma_z + \frac{\partial G_{2,2}^{u_z}}{\partial \theta} \cos \gamma_z - \frac{G_{1,2}^{u_z} \sin \gamma_z + G_{2,2}^{u_z} \cos \gamma_z}{\tan \theta} \right), \\ \frac{\partial G_{1,2}^{u_z}}{\partial \phi} \frac{\sin \gamma_z}{\sin \theta} + \frac{\partial G_{2,2}^{u_z}}{\partial \phi} \frac{\cos \gamma_z}{\sin \theta} + \frac{G_{1,1}^{u_z} \sin \gamma_z + G_{2,1}^{u_z} \cos \gamma_z}{\tan \theta} \end{array} \right] \quad (13b)$$

The next step is to find the three positive eigenvalues ( $\lambda_h$ ;  $h=1,2,3$ ) of  $\bar{V}$  and their corresponding unit eigenvectors ( $\Lambda_{hm}$ ). These eigenvectors indicate strain rate patterns that are statistically uncorrelated; they have target amplitudes of  $\sum \dot{\epsilon}_m \Lambda_{hm}$  and standard deviations of  $\sqrt{\lambda_h}$ , respectively. Each of the three targets is now imposed as a scalar datum in the global system of equations. The corresponding coefficients of the nodal velocities are

$$\left. \begin{array}{l} f_{kj} = \frac{1}{R} \left[ \begin{array}{l} \frac{\partial G_{1,1}^j}{\partial \theta} \Lambda_{h1} + \frac{1}{2} \left( \csc \theta \frac{\partial G_{1,1}^j}{\partial \phi} + \frac{\partial G_{1,2}^j}{\partial \theta} - \frac{G_{1,2}^j}{\tan \theta} \right) \Lambda_{h2} \\ + \left( \csc \theta \frac{\partial G_{1,2}^j}{\partial \phi} + \frac{G_{1,1}^j}{\tan \theta} \right) \Lambda_{h3} \end{array} \right] \\ g_{kj} = \frac{1}{R} \left[ \begin{array}{l} \frac{\partial G_{2,1}^j}{\partial \theta} \Lambda_{h1} + \frac{1}{2} \left( \csc \theta \frac{\partial G_{2,1}^j}{\partial \phi} + \frac{\partial G_{2,2}^j}{\partial \theta} - \frac{G_{2,2}^j}{\tan \theta} \right) \Lambda_{h2} \\ + \left( \csc \theta \frac{\partial G_{2,2}^j}{\partial \phi} + \frac{G_{2,1}^j}{\tan \theta} \right) \Lambda_{h3} \end{array} \right] \end{array} \right\} \quad (14)$$

(Note that  $k$  equals  $h$  plus a constant that indicates how many data have previously been incorporated into the system.)

Once the global velocity solution has been found for any time step, it is necessary to do a local optimization calculation within each faulting element to find the predicted (model) rates  $p_z$  at which each fault ( $z=1, \dots, Z$ ) is slipping, as well as the residual strain rate  $\dot{\epsilon}_m^c$  which is due to deformation of the continuum around the faults. The total strain rate of the element must be the sum of the continuum and the fault contributions:

$$\dot{\epsilon}_m^c + \sum_{z=1}^Z H_{zm} p_z = \dot{\epsilon}_m \quad (15)$$

This problem is different from the global problem because the  $\dot{\epsilon}_m$  vector is known. Because of this constraint, it is an algebraic convenience to use the Lagrange multiplier method with three temporary weight variables ( $\zeta_1, \zeta_2$ , and  $\zeta_3$ ). Define the local score (in one element) that is to be optimized as

$$S' = - \sum_{z=1}^Z \frac{(p_z - s_z)^2}{(\delta s_z)^2} - \frac{\left( \dot{\epsilon}_1^{c^2} + \dot{\epsilon}_1^c \dot{\epsilon}_3^c + \dot{\epsilon}_3^{c^2} + \dot{\epsilon}_2^{c^2} \right)}{\mu_l^2} - \sum_{m=1}^3 \zeta_m \left( \dot{\epsilon}_m^c + \sum_{z=1}^Z H_{zm} p_z - \dot{\epsilon}_m \right) \quad (16)$$

where  $\delta s_z$  is the standard deviation of each slip rate according to the input data. Then, to find a local solution that has all fault rates as close as possible to their goals, while the continuum strain rate is close to zero and the total strain rate is correct, find the stationary point of  $S'$  with respect to variations in the  $p_z$ , the  $\dot{\epsilon}_m^c$ , and the  $\zeta_m$  in turn, leading to a linear system. The slip rate  $p_k^n$  that is finally recorded (for fault  $k$  in time step  $n$ ) is the average of the rates  $p_z$  in all the elements the fault passes through, where the averaging weights are the segment lengths  $\rho_{lz}$ .

The method described here for incorporating faults effectively multiplies each known fault offset into roughly 1~2 scalar data per finite element crossed by the trace. In addition, 1~2 pseudo data per element crossed are used to express the a priori assumption of continuum stiffness. Therefore, for parity between faulting elements and nonfaulting elements, the suggested value of  $W$  is the inverse of the mean area of finite elements.

#### A6. Use of Paleomagnetic Data

I assume that the paleomagnetic data set is restricted to sites that include some geologic or geochemical indication of the orientation of the paleohorizontal plane at the time of magnetization and that have been properly corrected for local structure. It is also best to exclude certain sedimentary rocks that are known to be especially prone to postmagnetization compaction, which can produce a nontectonic inclination anomaly.

The interpretation of paleomagnetic inclination and declination data in terms of north-south displacement and rotation requires the definition of a reference polar wander path. It is necessary to use the same velocity reference frame for polar wander and for velocity boundary conditions.

The inclination of a sample yields its magnetic paleolatitude according to a simple dipole model for the paleofield. This is converted to a paleolatitude anomaly by comparison with the polar wander path. Multiplying this paleolatitude anomaly by the radius of the planet and dividing by the length of time available results in the mean velocity component in the paleodirection of magnetic south (at the time of magnetization). This becomes the rate estimate  $r_k$ . For comparison, the model prediction is formed using

$$\left. \begin{array}{l} f_{kj} = G_{1,1}^j \cos \gamma - G_{1,2}^j \sin \gamma \\ g_{kj} = G_{2,1}^j \cos \gamma - G_{2,2}^j \sin \gamma \end{array} \right\} \quad (17)$$

and  $c_k = 0$ , where the nodal functions  $G_{x,y}^j$  are evaluated at the datum location and  $\gamma$  is the azimuth (measured clockwise) of north pointing paleomagnetic declinations (at the time of magnetization) with respect to present geographic north (in the reference frame of the undeformed part of the continent) at the datum location.



While the magnetic declination of a sample is clearly related to its history of rotation about a local vertical axis, the relationship is nonunique and model-dependent. In general, the declination anomaly can only be converted to a vertical-axis rotation if the displacement of the sample is negligible or approximately known. Here I assume that these questions have been resolved by the assumption or approximation most appropriate to the particular problem and that estimated net rotations about the local vertical axis ( $\Delta\gamma$ ) are available as input data. I also assume that the sense of large rotations has been decided in advance based on regional tectonics.

These values determine the average rotation rates  $r_k = \omega_k^{(\text{datum})} = \Delta\gamma/t$ , where  $\Delta\gamma$  is the vertical-axis rotation in going from past to present (counterclockwise positive) and  $t$  is the age of the magnetization. The interpretation of these rotations requires some assumptions about the shape and the stiffness of the bodies carrying the remnant magnetization; I assume that the outcrops selected for paleomagnetic sampling were rigid inclusions of equidimensional shape embedded in a deforming continuum. Therefore the rotation rate that the magnetization would be predicted to record is

$$p_k = \omega_k^{(\text{model})} = \frac{1}{2R} \left( \frac{w}{\tan\theta} + \frac{\partial w}{\partial\theta} - \csc\theta \frac{\partial v}{\partial\phi} \right). \quad (18)$$

Consequently, the model predictions are formed using  $c_k = 0$  and

$$\begin{aligned} f_{kj} &= \frac{1}{2R} \left( \frac{G_{1,2}^j}{\tan\theta} + \frac{\partial G_{1,2}^j}{\partial\theta} - \csc\theta \frac{\partial G_{1,1}^j}{\partial\phi} \right) \\ g_{kj} &= \frac{1}{2R} \left( \frac{G_{2,2}^j}{\tan\theta} + \frac{\partial G_{2,2}^j}{\partial\theta} - \csc\theta \frac{\partial G_{2,1}^j}{\partial\phi} \right). \end{aligned} \quad (19)$$

The methods described in sections A3 and A5 effectively multiply the continuum-stiffness assumption into one scalar datum per finite element and multiply each fault offset into 1–2 scalar data per finite element traversed. If the finite element grid has many elements, the paleomagnetic data will require a similar weighting in order to avoid being overwhelmed in the global solution. Accordingly, both  $f$  and  $g$  functions of (17) and (19) should be multiplied by a dimensionless weight factor  $P$  which is common to all paleomagnetic data. A suggested value for  $P$  is the square root of twice the number of finite elements, which is the mean number of elements traversed by a fault crossing the whole grid. Then, a paleomagnetic datum indicating an exotic terrane will receive the same procedural weight as a fault-offset datum on the terrane-bounding fault, and the outcome will depend on the relative values and their uncertainties. Different values of  $P$  can be used to investigate solutions in which paleomagnetic data are either less or more prominent.

#### A7. Use of Stress Directions

One principal stress direction must always be perpendicular to the free surface of the Earth or approximately vertical. Thus the orientation of the stress tensor is described by the azimuth ( $\gamma$ ; measured clockwise from north) of the most compressive horizontal principal stress ( $\hat{\sigma}_{1h}$ ). This direction

is geologically recorded as the strike of igneous dikes or other vertical veins that break through any laterally homogeneous, isotropic rock. In some cases, a population of faults with slickensides can be statistically analyzed to determine the stress direction [e.g., *Gephart, 1990*].

To relate this information about stress to my kinematic model, I approximate the lithosphere as horizontally isotropic, so that the principal directions of stress are the same as the principal directions of strain rate. There may be an error of up to 35° associated with this assumption; even so, I believe that the solutions will typically be more accurate and reasonable than those that ignore stress data.

Once we know the azimuth of  $\hat{\sigma}_{1h}$ , we can use this as the direction of a new local horizontal axis  $\hat{\alpha}$  and also define a perpendicular horizontal axis  $\hat{\beta}$  (right-handed;  $\hat{\alpha} \times \hat{\beta} = \hat{r}$ ). In these coordinates, the requirement that  $\hat{\alpha}$  is the most compressive horizontal principal strain rate direction can be stated in two parts:  $\dot{\epsilon}_{\alpha\beta} = 0$  and  $\dot{\epsilon}_{\alpha\alpha} < \dot{\epsilon}_{\beta\beta}$ . In terms of the global coordinate system, the first becomes

$$\dot{\epsilon}_{\theta\phi} \cos(2\gamma) + \frac{\dot{\epsilon}_{\theta\theta} - \dot{\epsilon}_{\phi\phi}}{2} \sin(2\gamma) = 0. \quad (20)$$

In terms of derivatives of velocity, this is

$$\begin{aligned} \frac{1}{2R} \left\{ \left( \csc\theta \frac{\partial v}{\partial\phi} + \frac{\partial w}{\partial\theta} - \frac{w}{\tan\theta} \right) \cos(2\gamma) + \right. \\ \left. \left( \frac{\partial v}{\partial\theta} - \csc\theta \frac{\partial w}{\partial\phi} - \frac{v}{\tan\theta} \right) \sin(2\gamma) \right\} = 0, \end{aligned} \quad (21)$$

so the coefficients of the linear system can be computed from the factors

$$\begin{aligned} f_{kj} &= \frac{1}{2R} \left\{ \left( \csc\theta \frac{\partial G_{1,1}^j}{\partial\phi} + \frac{\partial G_{1,2}^j}{\partial\theta} - \frac{G_{1,2}^j}{\tan\theta} \right) \cos(2\gamma) + \right. \\ &\quad \left. \left( \frac{\partial G_{1,1}^j}{\partial\theta} - \csc\theta \frac{\partial G_{1,2}^j}{\partial\phi} - \frac{G_{1,1}^j}{\tan\theta} \right) \sin(2\gamma) \right\} \\ g_{kj} &= \frac{1}{2R} \left\{ \left( \csc\theta \frac{\partial G_{2,1}^j}{\partial\phi} + \frac{\partial G_{2,2}^j}{\partial\theta} - \frac{G_{2,2}^j}{\tan\theta} \right) \cos(2\gamma) + \right. \\ &\quad \left. \left( \frac{\partial G_{2,1}^j}{\partial\theta} - \csc\theta \frac{\partial G_{2,2}^j}{\partial\phi} - \frac{G_{2,1}^j}{\tan\theta} \right) \sin(2\gamma) \right\} \end{aligned} \quad (22)$$

if we use  $c_k = 0$  and a rate estimate  $r_k = 0$ . The difficulty is in deciding what standard deviation  $\sigma_k$  to associate with this constraint  $\dot{\epsilon}_{\alpha\beta} = 0$ , since we have transformed the constraint from one concerning an angle to one concerning a strain rate component. When the calculation is first starting and there are no strain rates known as yet, a purely arbitrary small strain rate uncertainty ( $\xi$ ) must be assigned as  $\sigma_k$ . However, when strain rate estimates are available from a previous time step (or from a previous iteration of the current time step), it is better to use  $\sigma_k = 2(\delta\gamma)(\dot{\epsilon}_{\theta\phi}^2 + (\dot{\epsilon}_{\theta\theta} - \dot{\epsilon}_{\phi\phi})^2/4)^{1/2}$ , where the symbol  $\delta\gamma$  indicates the standard deviation (in radians) of the azimuth  $\gamma$  of the direction  $\hat{\sigma}_{1h}$ . This suggests that the ve-

locity solution should be iterated within each time step; in this project I have used four iterations per time step.

The second requirement was the inequality  $\dot{\epsilon}_{\alpha\alpha} < \dot{\epsilon}_{\beta\beta}$ . During each iteration of the solution, I evaluate the strain rates  $\dot{\epsilon}_{\alpha\alpha}$  and  $\dot{\epsilon}_{\beta\beta}$  to see if this is true. If not, then in future iterations I impose an additional constraint  $\dot{\epsilon}_{\beta\beta} = \dot{\epsilon}_{\alpha\alpha} + \xi$ , where  $\xi$  is a small (positive) strain rate difference which must be arbitrarily chosen. In terms of the global coordinates,

$$(\dot{\epsilon}_{\phi\phi} - \dot{\epsilon}_{\theta\theta})\cos(2\gamma) + 2\dot{\epsilon}_{\theta\phi}\sin(2\gamma) = \xi. \quad (23)$$

This can be expressed in terms of velocity components as

$$\frac{1}{R} \left\{ \begin{array}{l} \left( \csc\theta \frac{\partial w}{\partial \phi} + \frac{v}{\tan\theta} - \frac{\partial v}{\partial \theta} \right) \cos(2\gamma) + \\ \left( \csc\theta \frac{\partial v}{\partial \phi} + \frac{\partial w}{\partial \theta} - \frac{w}{\tan\theta} \right) \sin(2\gamma) \end{array} \right\} = \xi, \quad (24)$$

so the coefficients of the linear system can be computed from the factors

$$\left. \begin{array}{l} f_{kj} = \frac{1}{R} \left\{ \begin{array}{l} \left( \csc\theta \frac{\partial G_{1,2}^j}{\partial \phi} + \frac{G_{1,1}^j}{\tan\theta} - \frac{\partial G_{1,1}^j}{\partial \theta} \right) \cos(2\gamma) + \\ \left( \csc\theta \frac{\partial G_{1,1}^j}{\partial \phi} + \frac{\partial G_{1,2}^j}{\partial \theta} - \frac{G_{1,2}^j}{\tan\theta} \right) \sin(2\gamma) \end{array} \right\} \\ g_{kj} = \frac{1}{R} \left\{ \begin{array}{l} \left( \csc\theta \frac{\partial G_{2,2}^j}{\partial \phi} + \frac{G_{2,1}^j}{\tan\theta} - \frac{\partial G_{2,1}^j}{\partial \theta} \right) \cos(2\gamma) + \\ \left( \csc\theta \frac{\partial G_{2,1}^j}{\partial \phi} + \frac{\partial G_{2,2}^j}{\partial \theta} - \frac{G_{2,2}^j}{\tan\theta} \right) \sin(2\gamma) \end{array} \right\} \end{array} \right\} \quad (25)$$

and  $c_k = 0$  if we create a new rate estimate  $r_k = \xi$ . The same value of  $\xi$  is also used to set the standard deviation for this constraint as  $\sigma_k = (0.83)\xi$ , so that the Gaussian distribution (which my method forces me to use) will best approximate the desired Heaviside distribution near the origin.

Paleostress data are different from structural and paleomagnetic data because they are not integral constraints over time but are momentary samples. A thin igneous dike may form in a day. Therefore it is necessary to distinguish between two types of published references on paleostress. The more desirable type summarizes many paleostress indicators of different ages to show that  $\hat{\sigma}_{1h}$  has remained constant over some time interval from age  $t_2$  to age  $t_1$ . These data should be applied in each time step of that interval ( $t_1/\Delta t < n \leq t_2/\Delta t$ ) with full relevance; that is,  $q_k^n = 1$ . The less desirable type of reference concerns paleostress indicators whose age can only be constrained to be less than  $t_2$  but more than  $t_1$ . These are relevant to one of the time steps in the interval, but it is not clear to which. These should be applied in all time steps of the interval but with reduced weight due to their reduced (mean) relevance; that is,  $q_k^n = \inf\{1, \Delta t/(t_2 - t_1)\}$ .

Ideally, very complete data sets on paleostress direction would impose a "smoothness" constraint on the velocity solutions, mimicking the smoothness that forward models have

as a result of solving the momentum equation. In practice, there are rarely more than a dozen relevant paleostress indicators in any given time step. A related problem is that if each paleostress indicator were only compared to the strain rate tensor in a single finite element, then its influence on the solution would decrease as the finite element grid was refined. I attempt to solve both problems by interpolating paleostress directions (with associated uncertainties) for every finite element in the grid, based on the relevant paleostress data. The interpolation is by nonparametric statistics based on the spatial autocorrelation of the present stress field as represented by the World Stress Map [Zoback, 1992]. The interpolation method is given by Bird and Li [1996]; I use the simpler of their two methods in which the data are considered independent, because this permits the weighting of the original data by their relevance ( $q_k^n$ ) values during the interpolation.

In cases where stress-direction data are sparse, it may be desirable or necessary to use active fault segments as additional indicators, assuming  $\hat{\sigma}_{1h}$  to be perpendicular to thrusts, etc. Only the first phase of movement on a fault should be used to indicate stress, because in later times the fault is an inherited plane of weakness.

#### A8. Integration Over Time

I use the "predictor/corrector" method of time integration, as in earlier forward dynamic models of the history of North America [Bird, 1988; 1992]. Each time step begins with an explicit "prediction" of new node locations. Using these, all nodal function derivatives, coefficients, and velocities are recomputed for the same time step. Then, the "predicted" velocity for that time step is "corrected" by adding one half of the (vector) change between the solutions. The node locations are corrected accordingly. Bird [1989] presented studies of the accuracy of this method; for practical purposes, it is sufficient to use time steps of ~1-5 m.y.

#### A9. Iterative Revision of Rate Histories

Because the events in geologic history that can be dated are not always those we would choose, many data about strain or displacement come with loose time windows, bracketing but not specifying the true duration of deformation. However, adjacent data with better constraints should cause strain rates to rise in the correct period. If the model-predicted rate for any datum is larger than the tentative goal rate, this is probably an indication that the goal rates for that datum should be revised to permit more rapid deformation in a portion of the time window.

My method is to assign new target rates  $(r_k^n)^*$  (for datum  $k$  in each time step  $n$ ), based on the predicted rates  $p_k^n$  from the previous model but adjusted by a constant factor to achieve the correct total strain, displacement, or rotation. Assuming a sign convention such that all goal rates are positive,

$$(r_k^n)^* = \left[ \frac{\sum_n r_k^n}{\sum_n \sup(p_k^n, 0)} \right] \sup(p_k^n, 0), \quad (26)$$

where the asterisk on the left indicates new goals for the next iteration, and all other quantities are old values from the pre-

vious iteration. (The truncation of the actual rates at zero is used in order to forestall a possible instability in the computation in which the denominator might become very small because of a predicted history that includes an unanticipated sense reversal.)

There are data for which this formula is inadequate: those whose time window extends back before the earliest time considered in the palinspastic reconstruction. My method for such cases is based on the assumption that strain and displacement in the earlier (unmodeled) period had the same sign as the net strain or displacement in the time period of the model. Therefore, if the model predicts too much total strain in the modeled interval, the targets must be reduced using (26) in order to prevent implied earlier rates from switching sign. However, if the model predicts too little strain, then the targets are not adjusted, because strain of the same sense in the unmodeled period can make up the difference.

Another possible problem with method (26) is that in some cases it can cause numerical instability (i.e., self-amplification of small rate variations). The method is stable when applied to data with a constructive interaction (e.g., two fault segments that together form a microplate boundary), neutrally stable for isolated data that interact only with the a priori stiffness, and unstable for groups of data with a destructive interaction (e.g., two parallel thrust faults). In the unstable case, the repeated application of (26) leads to a history in which only one of the data has a nonzero rate in any particular time step. This is undesirable because the details of their rate histories arise from the solution process and not from the data. To prevent this, I only apply (26) to those data (and in those iterations) where the predicted rate in at least one time step exceeds the corresponding goal rate; this is a sign of a constructive interaction.

The entire computation is now repeated, beginning at the present. In many cases, data that have tight time constraints are able to pinpoint the time of an orogeny locally, but their influence is diluted by other data with broad time windows. Thus the peak in strain rate (as a function of time) in the computed history is initially modest. However, with iteration the tentative rates for the latter data will be adjusted to reflect a shorter, more intense event.

#### A10. Idealized Test Cases

The program Restore (Appendix B) which realizes this algorithm has been successfully tested in the following cases:

1. With no data except the a priori constraint and with a few boundary nodes fixed, the grid remains static.

2. With no data except the a priori constraint and with velocity boundary conditions at two nodes that imply plate rotation about a local Euler pole, the grid rotates as a rigid plate with no deformation. During rotation at angular rate  $10^{-15} \text{ s}^{-1}$ , internal strain rates are less than  $2 \times 10^{-19} \text{ s}^{-1}$ .

3. Rotation of this "rigid" plate through finite time steps does not add significant error. For example, when the whole grid is rotated  $60^\circ$  in steps of  $6^\circ$  around a local Euler pole with the predictor/corrector method, all fictitious strains are  $\leq 0.8\%$ , much less than the fictitious strains of  $5.6\% = [\cos(6^\circ)]^{-10} - 1$  that would result from explicit time integration.

4. Regions with no data behave as isotropic sheets of incompressible viscous material when forced to deform. For example, when a domain of  $27^\circ$  longitude range and  $10^\circ$  latitude range lying along the equator is stretched E-W, the strain in the center can be described by  $\epsilon_{\theta\theta} = \epsilon_{rr} = -\epsilon_{\phi\phi}/2$ . When the uncertainty of the a priori zero strain rate ( $\mu$ ) is laterally heterogeneous, computed strain rates ( $\dot{\epsilon}$ ) are higher in regions of higher  $\mu$ . However, the scaling in this case is  $\dot{\epsilon} \sim \mu^2$ , not  $\dot{\epsilon} \sim \mu$  as one might guess.

5. When a single strike-slip fault that is an arc of a small circle cuts across the domain from one side to the other, the resulting solution has relative rotation of two rigid plates about the pole of the small circle. When a single dip-slip fault that is an arc of a great circle cuts across the domain from one side to the other, the resulting solution has relative rotation of two rigid plates about a point  $90^\circ$  away on the great circle.

6. When an active fault terminates in the model interior there is a conflict between the datum showing fault activity and the a priori assumption of no intraplate deformation. If the plate stiffness ( $W/\mu^2$ ) is small and the fault's slip rate uncertainty ( $\delta s$ ) is also small, then the reduction in slip rate is negligible. If both parameters are large, the fault may nearly be prevented from slipping.

A quantitative measure of this effect can be derived from the analytic solution of a simpler problem. Assume that an inverse model makes only one scalar prediction ( $p$ ) which is to be compared with all data. These data include  $N_r$  entries showing a positive rate of  $r$  with uncertainty  $\sigma_r$  and  $N_0$  entries showing a rate of zero with uncertainty  $\sigma_0$ . If we define a dimensionless parameter

$$\Gamma \equiv \frac{N_r \sigma_0^2}{N_0 \sigma_r^2} \quad (27)$$

then the result of a maximum-likelihood solution is

$$\frac{p}{r} = \frac{\Gamma}{\Gamma + 1} \quad (28)$$

This case is more complicated because the model predicts a range of slip rates along the fault trace and a range of continuum strain rates in its neighborhood. However, the scaling is  $N_r \sim \sum \kappa_{\ell z}$  (the number of finite elements crossed by the fault);  $N_0 \sim WI^2$  (where  $I$  is the length of the fault trace);  $\sigma_r \sim \delta s$ ; and  $\sigma_0 \cong \mu I$ . Together these suggest a new dimensionless parameter

$$\Gamma_f \equiv \tau \frac{\mu^2 \sum_{\ell=1}^L \kappa_{\ell z}}{(\delta s)^2 W} \quad (29)$$

in which  $\tau$  is a dimensionless coefficient which depends on the type of faulting. Numerical tests with one isolated fault in the middle of a plate show that these equations give good predictions of mean slip rate (within 5%) if the following coefficients are used: strike slip  $\tau_s \cong 1.0$ ; thrust  $\tau_t \cong 0.2$ ; normal  $\tau_n \cong 5$ ; and detachment  $\tau_d \cong 1.0$ .

7. In order to test the iteration of the tectonic history with (26), I divided the domain into two plates with one great circle strike-slip fault. Then, I artificially segmented the fault, assigning the same offset to each segment but assigning dif-

ferent (overlapping) time windows for slip on each segment. With iteration, the algorithm slowly converged on the correct solution, in which the slip history is the same for all segments, with all slip taking place within the shortest of the time windows. If the assigned uncertainties in fault slip rate are small and/or the continuum stiffness ( $W/\mu^2$ ) is low, then convergence is slow, because actual slip rates are only slightly different from goal rates, and hence the goals are only adjusted in small steps. Scaling suggests that the number of iterations required for convergence should be proportional to  $(\Gamma_f + 1)$ , and numerical trials confirm this. Thus there is a trade-off between fitting the data closely and converging quickly on the best deformation history. A good computational strategy is to set the parameters for small values of  $\Gamma$  ( $\cong 1-3$ ) in the early iterations, then to raise  $\Gamma$  in later iterations; such a method is similar to simulated annealing.

8. Balanced cross section data yield the correct relative displacement of their endpoints when there is no conflict with other data. For example, when two cross sections each span a long thrust fault with very uncertain offset (e.g.,  $\sigma = 1000$  km), they determine its slip distribution and also determine the relative rotation of the rigid plates on each side.

9. If a single cross section with nonzero extension is located in a plate interior away from any faults or other data, there is a conflict between the cross-section datum and the a priori assumption of no intraplate deformation. I have found a dimensionless parameter for cross sections,

$$\Gamma_c \equiv \tau_c \frac{\mu^2}{\sigma_c^2 W} \quad (30)$$

in which  $\sigma_c$  is the uncertainty of the extension rate of the cross-section. Used with equation (28), this parameter gives a good prediction of model rates of cross-section extension when the nondimensional factor  $\tau_c = 0.8$ .

10. When several cross sections showing equal shortening (or extension) are placed en echelon in a band (like stitches), they overcome the a priori constraint of plate rigidity and define a band of orogeny (or taphrogeny). In order for the far-field velocity difference to be similar to the shortening (extension) velocity along each cross section, the spacing between cross sections must be comparable to their individual lengths or less.

11. When a microplate is completely free to move (e.g., isolated from the boundary conditions by a small-circle strike-slip fault of unknown offset) and it contains a paleolatitude anomaly datum, the microplate moves toward or away from the paleopole in accordance with the datum.

12. When a paleomagnetic site with a paleolatitude anomaly occurs in a plate interior isolated from active faults or other data, there is a conflict with the a priori assumption of no deformation, and the solution is a compromise. There is a dimensionless factor for paleolatitude anomalies

$$\Gamma_p \equiv \tau_p \frac{\mu^2 P}{\sigma_p^2 W} \quad (31)$$

(where  $\sigma_p$  is the uncertainty in the mean N-S velocity in  $\text{m s}^{-1}$ , and  $\tau_p \cong 1$ ) which can be used with (28) to predict the result. For example, with typical values  $P = 100$ ,  $W = 1 \times 10^{-10}$

$\text{m}^{-2}$ , and  $\sigma_p = 6 \times 10^{-10} \text{ m s}^{-1}$  ( $5^\circ$  per 30 m.y.), the N-S motion of the site will only exceed half its nominal value for  $\mu > 5 \times 10^{-16} \text{ s}^{-1}$ ; this is a large value that might be assigned in British Columbia but would not be appropriate in Wyoming.

13. When a plate containing a single paleomagnetic site indicating a vertical-axis rotation is constrained at only one node, it rotates at the correct rate without negligible internal deformation.

14. When an paleomagnetic site showing vertical-axis rotation occurs in a plate interior isolated from active faults or other data, there is a conflict with the a priori assumption of no deformation, and the solution is a compromise. There is a dimensionless factor for rotation data

$$\Gamma_r \equiv \tau_r \frac{\mu^2 P}{\sigma_r^2 W a} \quad (32)$$

(where  $\sigma_r$  is the uncertainty in the rotation rate in radians per second,  $a$  is the area of a typical finite element, and  $\tau_r \cong 0.2$ ) which can be used with (28) to predict the result.

15. If uniform stress-direction data are given for each element in a problem where other data do not completely dictate the stress direction, then the velocity solution changes to honor the stress constraints. One problem tested had a rectangular plate fixed on its eastern side and forced to deform by several paleomagnetic sites with equal latitude anomalies along its western edge. If the stress direction was not constrained, the solution was a combination of dextral simple shear and clockwise rotation. If N-S  $\sigma_{1h}$  was specified, the solution changed to a combination of dextral simple shear and E-W extension, with little rotation. Three refinements of the velocity solution were enough for convergence.

#### A11. Assignment of Uncertainties to Rate Estimates

Most structural and paleomagnetic data indicate that some strain or displacement (symbolized here by the generic  $\varepsilon$ ) occurred after time  $t_2$  and before time  $t_1$ . They do not imply that the rate was constant during that period. The computation begins by using the average rate as the rate estimate in each time step (except less at each end):

$$r_k^n = \frac{\varepsilon_k}{(t_2 - t_1)_k} \frac{\inf \left\{ \begin{array}{l} \Delta t, \\ n \Delta t - (t_1)_k, \\ (t_2)_k - (n-1) \Delta t \end{array} \right.}{\Delta t} \quad (33)$$

However, it would be inadequate to estimate the rate uncertainties  $\sigma_k^n$  by dividing the standard deviation of the deformation ( $\delta \varepsilon_k$ ) by the time interval  $(t_2 - t_1)_k$ . That would confuse the uncertainty in the rate during one time step with the uncertainty in the average rate. Also, it would have the perverse effect of making data less important as their geologic age constraints became tighter.

A related practical problem concerns the convergence of the iteration process by which we attempt to revise the rate histories (26). Fault offsets are often known with very small uncertainties. If the offset uncertainty is the only contribution to  $\sigma_k^n$ , then the rate uncertainty is so small that the model

prediction of the rate is virtually identical to the rate goal. Therefore the adjustment of the rate history is unacceptably slow.

My solution is to begin the iteration process with a standard rate uncertainty  $\sigma^*$  assigned to each datum in a homogeneous class. This value is chosen so as to give  $\Gamma$  values of order unity for all data. This permits the data to interact and permits adjustment of some rate histories in a reasonable number of iterations. Then, as the iteration continues, the rate uncertainties are gradually changed to values based only on the uncertainties in the numerators according to

$$\left(\sigma_k^n\right)_i = \sigma^* \left[ \frac{1}{\sigma^* (t_2 - t_1)_k} \right]^{(i-1)}, \quad (34)$$

(for all  $n$  and for all  $k$  in the class) where  $i$  is the iteration number up to a maximum of  $M$ . One way to think of this is that (most) rate uncertainties are initially increased arbitrarily to allow for the uncertainty in the time-history, or denominator. Once the time-history has been adjusted, they are smoothly returned to values based only on their numerators. Another way to say this is that the algorithm begins with a least squares solution, passes through a phase of weighted least squares solutions, and finishes with a maximum-likelihood solution.

## Appendix B: Program and Data Files Available

The following computer files include everything needed to reproduce the computation and also to track the geologic data to its sources in the literature. These files will be available indefinitely for anonymous FTP access at the Internet address (URL) of <ftp://element.ess.ucla.edu/restore>.

Restore.f90	Fortran 90 source code for program Restore, version 2.0;
Parameters.dat	short file of input parameters (read by Restore);

## References

- Avouac, J P, and P. Tapponnier, Kinematic model of active deformation in Central Asia, *Geophys. Res. Lett.*, 20, 895-898, 1993
- Bazard, D R, and R F. Butler, Paleomagnetism of the Chinle and Kayenta formations, New Mexico and Arizona, *J. Geophys. Res.*, 96, 9847-9871, 1991
- Bird, P., Formation of the Rocky Mountains, western United States a continuum computer model, *Science*, 239, 1501-1507, 1988
- Bird, P., New finite element techniques for modeling deformation histories of continents with stratified temperature-dependent rheologies, *J. Geophys. Res.*, 94, 3967-3990, 1989.
- Bird, P., Deformation and uplift of North America in the Cenozoic era, in *Scientific Excellence in Supercomputing: The IBM 1990 Contest Prize Paper*, vol. 1, edited by K.R Billingsley, H.U Brown III, and E Derohanes, pp. 67-105, Baldwin Press, Athens, Ga., 1992
- Bird, P., and Y. Li, Interpolation of principal stress directions by nonparametric statistics Global maps with confidence limits, *J. Geophys. Res.*, 101, 5435-5443, 1996.
- Bryan, P., and R G. Gordon, Rotation of the Colorado Plateau An updated analysis of paleomagnetic poles, *Geophys. Res. Lett.*, 17, 1501-1504, 1990
- Burchfiel, B C, and G A Davis, Nature and controls of cordilleran orogenesis, western United States Extensions of an earlier synthesis, *Am. J. Sci.*, 275-A, 363-396, 1975
- Chapin, C E, An overview of Laramide wrench faulting in the southern Rocky Mountains with emphasis on petroleum exploration, in *Rocky Mountain Foreland Basins and Uplifts*, edited by JD Lowell and R Gries, pp 169-180, Rocky Mt Assoc. of Geol., Denver, Colo., 1983
- Chapin, C. E., and S M Cather, Eocene tectonics and sedimentation in the Colorado Plateau-Rocky Mountain area, *Ariz. Geol. Soc. Dig.*, 14, 173-198, 1981
- Constenius, K N (1996) Late Paleogene extensional collapse of the Cordilleran fold and thrust belt, *Geol. Soc. Am. Bull.*, 108, 20-39.
- DeCelles, P. G., and G. Mitra, History of the Sevier orogenic belt in terms of critical taper models, northeast Utah and southwest Wyoming, *Geol. Soc. Am. Bull.*, 107, 454-462, 1995
- Dickinson, W R., and W S Snyder, Plate tectonics of the Laramide orogeny, in *Laramide Folding Associated with Basement Block Faulting in the Western United States*, edited by V Matthews III, *Mem Geol Soc. Am.*, 151, 355-366, 1978
- Dickinson, W R., and W S Snyder, Geometry of subducted slabs related to San Andreas transform, *J. Geol.*, 87, 609-627, 1979
- Dickinson, W R., M A Klute, M J Hayes, S. U Janecke, E R Lundin, M A McKittrick, and M D Olivares, Paleogeographic and paleotectonic setting of Laramide sedimentary basins in the central Rocky Mountain region, *Geol. Soc. Am. Bull.*, 100, 1023-1039, 1988
- Engelbreton, D C, A Cox, and R G Gordon, Relative motions between oceanic and continental plates in the Pacific basin, *Spec. Pap Geol Soc Am*, 206, 59 pp., 1985
- Gephart, J. W., Stress and the direction of slip on fault planes, *Tectonics*, 9, 845-858, 1990
- Gries, R., North-south compression of Rocky Mountain foreland structures, in *Rocky Mountain Foreland Basins and Uplifts*, edited by J D Lowell and R. Gries, pp 9-32, Rocky Mt Assoc. Geol., Denver, Colo., 1983.
- Hamilton, W., Plate-tectonic mechanism of
- fRMF.xls table of information about fault offsets, including references to literature, with my editorial summation (Microsoft Excel file);
- fRMF.dat table of fault offsets, with my editorial summation of timing and uncertainties but without references to literature (read by Restore);
- fRMF.dig digitized traces of faults (read by Restore);
- cRMF.dat table of restored lengths of balanced cross sections, with references (read by Restore);
- pRMF.dat table of paleomagnetic sites with inferred paleolatitude anomalies and vertical-axis rotations and original references (read by Restore);
- sRMF.dat table of paleostress direction indicators with original references (read by Restore);
- RMF7.feg finite element grid (read by Restore);
- RMF7.bcs boundary conditions for finite element grid (read by Restore);
- RMF\_refs.txt bibliographic citations for all references in the data tables, except for entries in pRMF.dat that begin "IAGA"; for these, the source were listed by *McElhinny and Lock* [1995].

- Laramide deformation, in *Rocky Mountain Foreland Basement Tectonics*, edited by D W Boyd and J. A. Lillegraven, *Contrib. Geol.*, **19**, 87-92, 1981
- Heller, P. L., and C Paola, The paradox of Lower Cretaceous gravels and the initiation of thrusting in the Sevier orogenic belt, United States western interior, *Geol. Soc. Am. Bull.*, **101**, 864-875, 1989
- Henderson, L. J., R. G. Gordon, and D. C. Engbreton, Mesozoic aseismic ridges on the Farallon plate and southward migration of shallow subduction during the Laramide orogeny, *Tectonics*, **3**, 121-132, 1984
- Holt, W. E., and A. J. Haines, Velocity fields in deforming Asia from the inversion of earthquake-related strains, *Tectonics*, **12**, 1-20, 1993.
- Jurdy, D. M., The subduction of the Farallon plate beneath North America as derived from relative plate motions, *Tectonics*, **3**, 107-113, 1984
- Kent, D. V., and W. K. Witte, Slow apparent polar wander for North America in the Late Triassic and large Colorado Plateau rotation, *Tectonics*, **12**, 291-300, 1993.
- Kong, X. and P. Bird, SHELLS: A thin-shell program for modeling neotectonics of regional or global lithosphere with faults, *J. Geophys. Res.*, **100**, 22,129-22,131, 1995.
- Livaccari, R. F., Role of crustal thickening and extensional collapse in the tectonic evolution of the Sevier-Laramide orogeny, western United States, *Geology*, **19**, 1104-1107, 1991
- Livaccari, R. F., K. Burke, and A. M. C. Sengor, Was the Laramide orogeny related to the subduction of an oceanic plateau?, *Nature*, **289**, 276-278, 1981.
- Maxson, J., and B. Tikoff, Hit-and-run collision model for the Laramide orogeny, western United States, *Geology*, **24**, 968-972, 1996
- McElhinny, M. W., and J. Lock, Four IAGA paleomagnetic databases released in one package, *Eos Trans. AGU*, **76**, 266, 1995
- Molina Garza, R. S., G. D. Acton, and J. W. Geissman, Carboniferous through Jurassic paleomagnetic data and their bearing on rotation of the Colorado Plateau, *J. Geophys. Res.*, in press, 1998
- Peltzer, G., and F. Saucier, Present-day kinematics of Asia derived from geologic slip rates, *J. Geophys. Res.*, **101**, 27,943-27,956, 1996.
- Saucier, F., and E. Humphreys, Horizontal crustal deformation in southern California from joint models of geologic and very long baseline interferometry measurements, in *Contributions of Space Geodesy to Geodynamics: Crustal Dynamics, Geodyn. Ser.*, vol. 23, edited by D. E. Smith and D. L. Turcotte, pp. 139-176, AGU, Washington, D. C., 1993
- Snyder, W. S., W. R. Dickinson, and M. L. Silberman, Tectonic implications of space-time patterns of Cenozoic magmatism in the western United States, *Earth Planet. Sci. Lett.*, **32**, 91-106, 1976.
- Steiner, M. B., Rotation of the Colorado Plateau, *Tectonics*, **5**, 649-660, 1986.
- Tikoff, B., and M. de Saint Blanquat, Transpressional shearing and strike-slip partitioning in the Late Cretaceous Sierra Nevada magmatic arc, California, *Tectonics*, **16**, 442-459, 1997
- Urrutia-Fucugauchi, J., Late Mesozoic-Cenozoic evolution of the northwestern Mexico magmatic arc zone, *Geof. Int.*, **25-1**, 61-84, 1986
- Van Alstine, D. R., and J. de Boer, A new technique for constructing apparent polar wander paths and the revised Phanerozoic path for North America, *Geology*, **6**, 137-139, 1978
- Woodward, L. A., O. J. Anderson, and S. G. Lucas, Mesozoic stratigraphic constraints on Laramide right slip on the east side of the Colorado Plateau, *Geology*, **25**, 843-846, 1997
- Zienkiewicz, O. C., *The Finite Element Method in Engineering Science*, 521 pp., McGraw-Hill, New York, 1971
- Zoback, M. L., First- and second-order patterns of stress in the lithosphere: The World Stress Map Project, *J. Geophys. Res.*, **97**, 11,703-11,728, 1992

---

P. Bird, Department of Earth and Space Sciences, University of California, Los Angeles, CA 90095-1567 (pbird@ess.ucla.edu)

(Received January 6, 1998,  
revised July 17, 1998,  
accepted August 18, 1998.)